Universal rhythmic architecture uncovers distinct modes of neural dynamics

Golan Karvat [1]*, Maité Crespo-García [1], Gal Vishne [2], Michael C Anderson [1]†, Ayelet N Landau [3,4,5]†

[1] MRC Cognition and Brain Sciences Unit, University of Cambridge; Cambridge CB2 7EF, United Kingdom.
[2] Edmond and Lily Safra Center for brain sciences, The Hebrew University of Jerusalem; Jerusalem 9190401, Israel.
[3] Department of Psychology, The Hebrew University of Jerusalem; Jerusalem 9190401, Israel.
[4] Department of Cognitive and Brain Sciences, The Hebrew University of Jerusalem; Jerusalem 9190401, Israel.
[5] Department of Experimental Psychology, University College London (UCL); London WC1H 0AP, United Kingdom.
† Co-senior author.

* Contact: Golan Karvat Correspondence: golan.karvat@mrc-cbu.cam.ac.uk

December 03, 2024. Preprint v1.1

Understanding the organizing principles of brain activity can advance neuro-technology and medical diagnosis and treatment. A prominent principle promoted over the last century is that brain activity consists of electrical field potentials that oscillate at different frequency bands. However, this principle has been challenged on several grounds. Specifically, increasing evidence suggests that in some cases brain oscillations are manifested as transient bursts rather than sustained rhythms. In this paper, we examine the hypothesis that rhythmicity (sustained vs. bursty) is an additional dimension in the organization of brain function. To test this hypothesis, we segmented the neurophysiological spectrum of 859 participants encompassing a dozen datasets across species, recording techniques, ages 18-88, brain regions, and cognitive states in both health and disease, according to a novel measure of rhythmicity. Together with computer simulations and brain stimulation, we found a universal spectral architecture divisible into two categories: high-rhythmicity bands associated with sustained oscillations and novel low-rhythmicity bands dominated by brief oscillatory bursts. This universal architecture reveals stable features of the brain's mode of operation: sustained bands signify maintenance of ongoing activity, whereas transient bands signify the brain's response to change. Rhythmicity specifies a powerful, replicable, and accessible feature-set for neuro-technology and diagnosis, as well as cross-species comparisons.

Understanding the organizing principles of the brain's electrical activity using non-invasive techniques is a major goal of neuroscience, with implications for brain-computer interface (BCI) design, pathology diagnosis, and treatment. A dominant hallmark of the electrophysiological signal is its tendency to oscillate. These oscillations are thought to signify synchronized fluctuations in neuronal excitability, present in neuronal systems from rodents to humans, and can be detected invasively or non-invasively (*1*, *2*). According to a current viewpoint, the entire electrophysiological spectrum is composed of oscillatory bands, covering all frequencies from 0.1 to more than 100 Hz (*3*) [the "canonical bands" delta (0.1-4 Hz), theta (4-8 Hz), alpha (8-13 Hz), beta (13-30 Hz), gamma (30-80 Hz), and high-frequency oscillations (80-250 Hz)]. A century of research and thousands of studies suggest that these seamlessly progressing bands form the spectral architecture of the brain, with oscillatory activity in different bands supporting distinct cognitive and physiological states (*4*, *5*). This spectral architecture is now considered as one of the fundamental principles of neuronal activity (*2*). However, several practical, functional, and physiological considerations challenge this viewpoint, calling for a revision of this architecture.

On the practical level, band definitions vary widely between research-groups (*6*), which limits our ability to compare findings between studies and species. In addition, bands are currently defined and identified by sustained oscillatory activity and, as such, are assumed to progress seamlessly at the group level. However, at the single-subject level, which is vital for individualized neurotechnology, diagnosis, and treatment, these relatively wide bands consist of aperiodic activity and some narrow band oscillations (*7*). With no objective framework for relating non oscillatory activity to canonical frequency bands, the role of activity within these gaps, if any, remains unknown. On the functional level, at least two of the canonical bands (beta and gamma) are thought to contain sub-bands with distinct, and even opposing, roles (*8*, *9*), indicating the need for a more nuanced characterization of bands. On the physiological level, increasing evidence indicates that some oscillatory responses are not sustained. Rather, they arise as strong, short-lived bursts (*10*–*12*). The bursts raise the possibility that the electrophysiological spectrum segregates into specialised frequency bands according to their persistence, i.e. sustained (referred to hereinafter as high-rhythmicity) versus bursty (low-rhythmicity) bands. To account for these challenges, we develop an objective standard to divide an individual's electrophysiological spectrum into high-rhythmic and low-rhythmic bands. We then show that the resulting novel architecture of high-rhythmic and low-rhythmic activity is universal and bears functional significance: rhythmic bands signify maintenance of ongoing activity, whereas non-rhythmic bands signify transient events.

Our hypothesis is thus that the brain uses both high-rhythmic and low-rhythmic activity. Such organization of spectral phenomena can bridge two prominent views of the brain's *modus operandi*, namely *phase-coding* (*13*) and *rate-coding* (*14*) (Fig. 1 panels A-B). These views differ regarding whether the precise timing of neuronal outputs encodes information about neuronal inputs. *Phase-coding* posits that oscillations temporally bias neuronal responses to inputs: synaptic inputs that arrive during the excitable phase of an oscillation are more likely to cause outputs; whereas inputs arriving at the opposite phase get dismissed or curtailed (*15*, *16*). According to this view, oscillations causally influence the formation, synchronization, and sequence of cell assemblies, communication efficacy, and ultimately, an organism's behaviour (*13*, *17–19*). In contrast, *rate-coding* proposes that the rate at which neurons "fire" electrical pulses called action potentials contains all relevant information. According to one interpretation of rate-coding (*14*), enhancing neuronal firing-rate suffices for assembly formation, deeming oscillations unnecessary. Indeed, we recently showed that momentary neuronal oscillations (bursts) occur together with transient firing-rate changes (*11*).

Combining insights from phase- and rate-coding, we hypothesized that both "sustained" and "bursty" bands exist and together comprise a universal rhythmicity architecture relevant to cognition by serving two modes of operation; sustained oscillations support phase-coding and maintenance of ongoing activity, whereas bursts reflect rate-coding and response to change. This hypothesis of rhythmicity serving as an additional dimension in the organization of brain function yields four testable predictions: (i) There should be defined frequency "sustained bands" that clearly express sustained oscillations. (ii) Additionally, there should be a separate, novel category of bands specializing in transient activity. In these "transient bands", spectral phenomena should manifest as short-lived bursts. (iii) The architecture is a universal organizing principle of the brain's operating system; hence it should arise across datasets, recording techniques, brain areas, and species. (iv) The architecture mediates cognition, hence its operation should be sensitive to variations in cognition arising with age and neuropathology, and to different cognitive states, such as input processing.

To test these predictions of our universal rhythmic architecture hypothesis, we developed a phase-based tool to measure rhythmicity over the frequency spectrum (Fig. 1C and fig. S1). Three features characterize brain oscillations: frequency (cycles per time-unit), power (or magnitude), and phase (or angle). The canonical bands are typically identified by measuring spectral power at different frequencies (fig. S2A-C). However, estimated power is influenced by both oscillatory activity and non-oscillatory transients. For example, a spectral power peak could result from strong im-

No.	Task/ population	Recording technique	N subjects	Recording sites	Age mean (range)	Ref.
I	Visual duration judgement	EEG	37 vol.	Cz	22.9 (18-29)	(*23*)
II	Eyes closed	EEG	37 vol.	Cz	22.9 (18-29)	(*23*)
III	Tactile duration judgement	EEG	29 vol.	Cz	24 (19-31)	(*24*)
IV	Audio–visual illusion	EEG	24 vol.	Cz	(18-42)	(*25*)
V	Memory-control	EEG	27 vol.	Cz	25 (20-34)	(*26*)
VI	Memory-control	HD-EEG	24 vol.	Cz	(18-35)	(*27*)
VII	TMS	EEG	6 vol.	F4	27 (19-37)	New
VIII	Rest	MEG	625 vol.	4 magnetometers surrounding Cz	(18-88)	(*28*)
IX	Epilepsy patients	ECoG	10 patients	867 electrodes (sites: Fig. 1I)	41 (19-65)	(*29*)
X	Epilepsy patients	EEG + SEEG	12 patients	733 electrodes (sites: Fig. 1J)	27.5 (17-39)	(*30*)
XI	PD patients	LFP	17 patients	STNs from 30 hemispheres	58 (48-65)	(*31*)
XII	Rats navigation	LFP	11 rats	Hippocampus		(*32*)

Table 1. Details of datasets used in this study.

No.: dataset number, EEG: electroencephalogram, HD-EEG: high-definition (high-channel-count) EEG, TMS: transcranial magnetic stimulation, MEG: magnetoencephalogram, ECoG: electrocorticography, SEEG: stereoelectroencephalogram (depth electrodes), LFP: local field potentials (depth electrodes), vol.: healthy human volunteers, Cz: midline central electrode, F4: right frontal electrode, Ref.: reference. PD: Parkinson's disease.

pulses which are not rhythmic. An alternative approach to power is to estimate how sustained the oscillation is by measuring how well, at any moment, the signal's phase predicts its future phase. This is achieved by computing the coherence, or phase similarity, between the signal and a time-lagged copy of itself. Previous studies measured the rhythmicity spectrum as a function of lag duration, assuming that genuine oscillations should remain sustained for many cycles (*20–22*). Here, based on large datasets and comprehensive simulations, we found that the relative rhythmicity *between* frequencies of individual subjects remains similar over lags. Hence, with carefully chosen parameters, the rhythmicity spectrum can be derived from a single lag (for further discussion, see Supplementary Text, parametrical effects on rhythmicity, and fig. S5). We term this algorithm the *lagged-angle vector index* (LAVI, Fig. 1C and fig. S1, supplementary materials, materials and methods). Beyond being an order of magnitude faster than previous lagged-coherence approaches, LAVI allows an automatic and statistically inferred detection of frequency bands at the individual subject level, of both increased and decreased rhythmicity. LAVI is therefore uniquely suited to testing our rhythmic-architecture hypothesis.

Universal rhythmic architecture

Establishing the rhythmic architecture as a universal phenomenon requires a robust, diverse, and large sample. Therefore, we computed the rhythmicity spectra of data from 12 datasets acquired from 2450 recording sites of 11 rats and 848 humans (with both invasive and non-invasive methods; Table 1). Using LAVI to measure rhythmicity, we established that the electrophysiological spectrum is divisible into significantly-high and significantly-low rhythmicity bands. A consistent architecture was found in all datasets, and across ages, species, brain regions, and recording techniques, in health and disease. When examining rhythmicity profiles, we noticed that LAVI values exhibit an evident baseline. The median (across frequencies) remained stable across participants, channels, and datasets, and depended on experimenter-controlled parameters (like lag duration and wavelet width, see details in supplementary text and fig. S5. With lag=1.5 cycles and wavelet width=5 cycles; non-invasive (datasets I-VIII): mean of medians: 0.41±0.01 SD, range: [0.38-0.45], n=809 participants; ECoG (dataset IX): 0.39±0.01 [0.35-0.43], n=867 electrodes; SEEG (dataset X): 0.40±0.01 [0.36-0.48], n=733 electrodes). Furthermore, median rhythmicity values of recorded data closely resembled median rhythmicity values of simulated data generated to match the power-spectra of recorded data but with random phases (fig. S2D and S5F-H). Leveraging this quality, we defined the median over frequencies as baseline rhythmicity, and the range of rhythmicity fluctuations of simulated (random-phase) data as "noise-ribbon". With these definitions, we devised an *automated band-border detection algorithm* (ABBA, Fig. 1D). Frequency bands with significantly high rhythmicity (p<0.05, Monte Carlo simulations) varied between individual subjects (fig. S2G), demonstrating the necessity for an objective band-detection framework. Nonetheless, the distribution of peak frequencies of each rhythmicity band across subjects conformed well with canonical, power-based bands (Fig. 1E) (*3*). This indicates that activity in canonical bands, traditionally defined as frequencies with high oscillatory power, indeed reflects rhythmically sustained signals.

Having confirmed the existence of sustained bands, we next examined whether transient bands exist. Using ABBA, we invariably found bands with significantly decreased phase-consistency, as expected from transient bands (Fig. 1F, fig. S3). We dub these bands "Delta/Theta (δ/θ)", "Theta/Alpha (θ/α)", "Beta1", and "Gamma1." To establish that this architecture of sustained and transient bands is universal, we computed the peak frequencies of these bands from a large body of data acquired using both invasive (ECoG, SEEG) and non-invasive (EEG, MEG) techniques. Then, we compared the rhythmicity architecture, expressed as the distributions of peak frequencies, across different datasets (EEG, Fig. 1G), age groups (MEG, Fig. 1H), and neuroanatomical locations (ECoG, Fig. 1I, SEEG, Fig. 1J). Using ABBA, we detected the canonical bands Theta, Alpha, and Beta2 in virtually all participants. Importantly, in the investigated frequency range (3-45 Hz) we found that transient bands were as common as sustained bands (datasets I-XI: Transient: 2.45 ± 0.03 (mean ± SEM) significant bands per participant, Sustained: 2.28 ± 0.02; dataset XIII: transient: 2.6 ± 0.03, sustained: 2.41 ± 0.03; dataset IX [per electrode]: transient: 2.17 ± 0.04, sustained: 2.31 ± 0.04; dataset X [per electrode]: transient: 2.22 ± 0.05, sustained: 2.44 ± 0.03). Bayes factor analysis (BF) indicated strong evidence for no difference in number of significant bands between the 6 different EEG datasets (BF_{01}=10.84). Importantly, our analysis is sensitive to within-bands variability, such as systematic age-related decrease in peak-frequency (Fig. 1H), thus can serve as a biomarker, consistent with (*33*).

Leveraging a unique recording setting including both scalp EEG and invasive electrodes in dataset X, we compared peak frequencies in invasive electrodes to peaks in the nearest EEG electrode. We found moderate evidence that scalp and intracranial values are similar ($BF_{10} < 1/2$, Fig. 1K). Furthermore, the invasive recordings from patients' hippocampi allowed us to compare the human rhythmic architecture to that of rat hippocampi. Similar to human datasets, we detected sustained and transient bands from Theta to Gamma1 in a majority of rats the 11 rats examined. Comparing bands' peak frequencies of signals recorded in the hippocampi of patients to hippocampal recordings from rats, we report moderate to strong evidence that the frequency distributions of bands from alpha to gamma1 are conserved from rats to humans (Fig. 1L). Taken together, the neurophysiological spectrum is divided into frequencies characterized with sustained oscillations and other frequencies characterized with transient oscillations. This rhythmicity architecture generalizes across datasets, brain regions, age, levels of invasiveness, and two mammalian species, consistent with the possibility of a universal architecture.

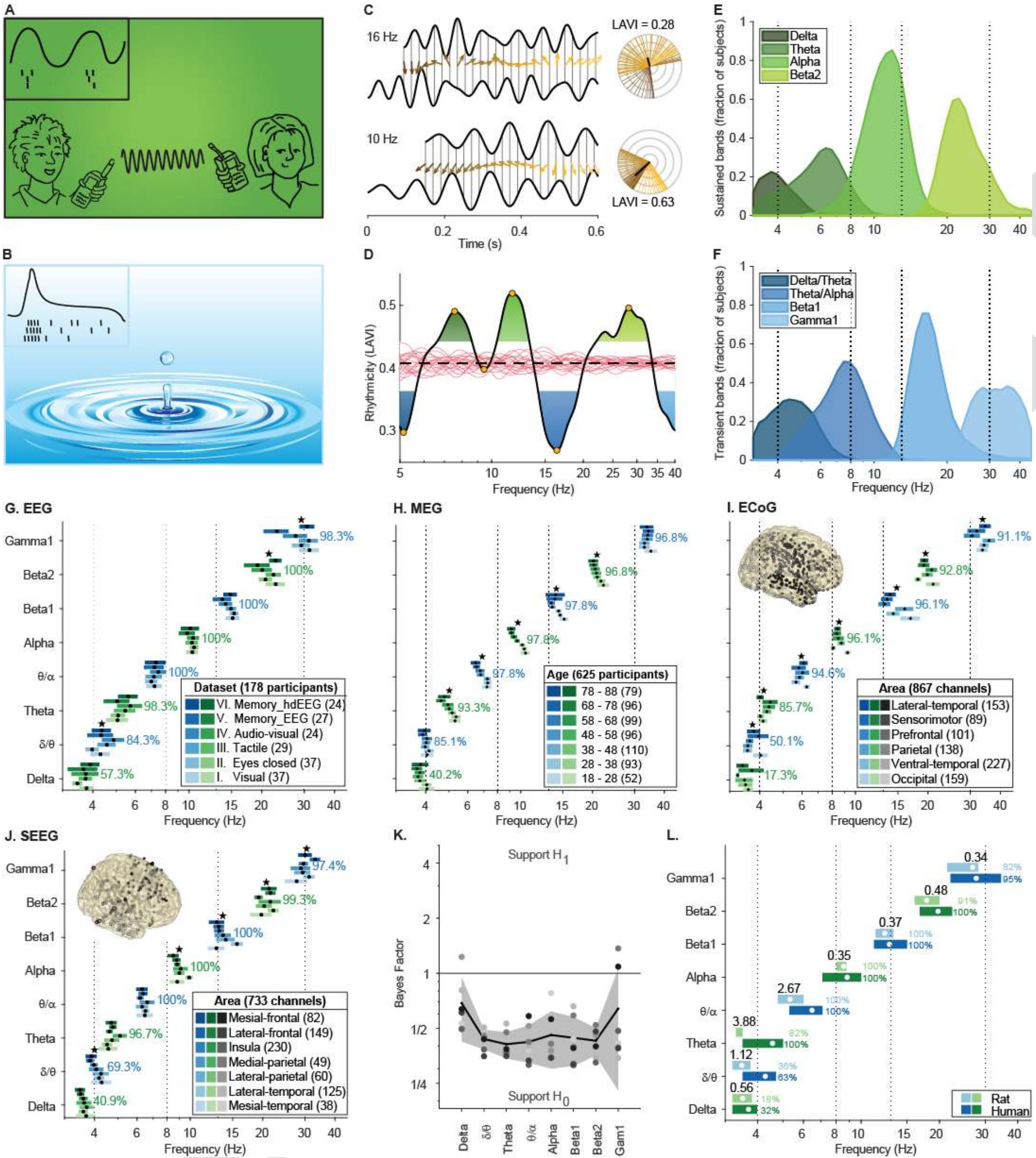

Fig. 1. Rhythmicity differentiates between brainwave modes. (**A-B**): Opposing views of neural coding. (**A**) Phase-code: oscillations synchronise neurons' firing (inset, wave represents field potential, ticks action-potentials of 3 neurons), thus enable efficient communication, like telecommunication devices exploit electromagnetic waves. (**B**) Rate-code: oscillations represent network's reverberation following a transient input, like ripples resulting from a drop of water. (**C**) To compute the Lagged Angle Vector Index (LAVI) in each frequency, the phase at each timepoint is subtracted from the phase of a lagged copy of the signal (arrows, colour represents time). LAVI is the vector sum of the differences in all timepoints (black lines, right circles). Rhythmic signals are expected to have consistent phases yielding large LAVI values, wihle non-rhythmic signals will yield lower LAVI values. (**D**) Rhythmicity profile of one subject and output of the Automated Band Border Algorithm (ABBA). Dashed line: median; pink traces: rhythmicity of 20 instantiations of simulated 1/f noise; gold circles: peaks and troughs; green (blue) filled areas: significantly increased (decreased) rhythmicity. (**E**) Population (N=90, datasets I, III, and IV) summary of significantly (*p*<0.05) rhythmically sustained bands detected by ABBA. For details on how bands are defined, see Supplementary Materials, Materials and Methods (Automated Band Border Algorithm). Dashed lines: borders between canonical bands (3). (**F**) Similar to (**E**), for significantly arrhythmic (transient) bands. (**G-L**): The rhythmicity architecture is universal. Peak frequencies in sustained (green) and transient bands (blue) in different EEG studies [(**G**), N participants per study appear in the legend], age groups [(**H**), measured using MEG, dataset VIII] and anatomical locations [(**I**), ECoG from dataset IX and (**J**), SEEG from dataset X, numbers in legends represent N electrodes]. Dots represent the mean and horizontal bars represent the 95% confidence interval per group/ area. Percent number next to each band represents the % of participants (**G, H**) or electrodes (**I, J**) with detected bands. Stars represent significant difference between datasets/ areas/ age-groups within a band (ANOVA; *p*<0.05). Note, that from theta to gamma, both transient and sustained bands are detected and predominantly do not overlap with neighbouring bands. (**K**) Comparison between peak-frequencies in SEEG electrodes and the nearest scalp EEG electrode in dataset X. Grey dots: areas as in (**J**). Line: mean. Shaded area: SD. (**L**). Comparison between human hippocampi SEEG (N=38) and LFP from rat hippocampi (N=11, dataset XII). Bayes factor analysis suggests moderate evidence for no difference between species in Alpha, Beta1, Beta2, and Gamma1. Note, that the ~8 Hz band is considered "Theta" in the publication of dataset XII. With LAVI analysis the highest peak was found at ~8 Hz, hence it was assigned to "Alpha" by ABBA. Dots: mean. Green (blue) horizontal lines: interquartile range of sustained (transient) bands. Artwork credit: Panel A was contributed to the manuscript by Mirjam Karvat. Panel B adapted from Allvectors.com under CC BY 4.0 licence.

Sub-second manifestations of rhythmicity

Our hypothesis posits that the universal rhythmic architecture supports both rate- and phase-coding, by allocating "bursty" activity to transient-bands, and "genuine" oscillations to sustained-bands. Testing this hypothesis requires linking the rhythmicity profiles (measured over minutes) to activity in the sub-second realm. To this end, we carried out two independent analyses and conducted a neuro-stimulation experiment. In the first analysis, we used standard burst detection algorithms (independent from LAVI, see methods) and examined whether bursts are shorter and more frequent in transient-bands compared to sustained-bands. Second, to complement the data-driven correlation between bursts and rhythmicity bands, we used simulations to test how sub-second parameters of the signal, and specifically burst-duration, influence the rhythmicity profile. Last, we sought causal evidence for the effect of bursts on rhythmicity. To this end, we used Transcranial Magnetic Stimulation (TMS) to deliver transient, rhythmic, and arrhythmic inputs, and asked how they affect the activity in different bands using a recently-reported time-resolved rhythmicity measure (namely Within-Trial Phase-Lock, WTPL (*23*)).

We defined oscillatory "bursts" as peaks in the time-frequency plane exceeding the 90th power percentile (*11*), while avoiding overlap in frequency and time between neighbouring bursts (supplementary materials, materials and methods). We then measured the rate of occurrence and mean duration of bursts in datasets I, III, and IV. Band category (transient or sustained) had a significant effect on both the rate and duration of bursts (ANOVA using category and band as groups, rate: category: $F_{1,439}=190.86$, $p<10^{-35}$, $\eta^2=0.30$; $BF_{10}=8.25*10^{32}$; band: $F_{5,435}=118.9$, $p<10^{-78}$, $\eta^2=0.58$; $BF_{10}=5.45*10^{22}$; duration: category: $F_{1,439}=123.7$, $p<10^{-24}$, $\eta^2=0.22$, $BF_{10}=1.66*10^{22}$; band: $F_{5,435}=72.2$, $p<10^{-54}$, $\eta^2=0.45$, $BF_{10}=31.26$, Fig. 2A, blue vs. green). Post-hoc Tukey Honest Significant Difference tests revealed higher burst-rates and shorter burst-durations in all transient bands compared to their neighbouring sustained bands. The increased rate and decreased duration of bursts in lower rhythmicity bands suggests that lower rhythmicity (stable over minutes) relates to transient activity in the sub-second realm (manifested by short-lived bursts).

We considered the possibility that the interaction between bands and burst levels results from a frequency-specific effect of random noise in the brain. In general, the power of the neurophysiological signal is inversely proportional to frequency, a phenomenon termed $1/f$. For each participant, we generated a matching surrogate dataset with random phases that matched their $1/f$ power profiles (methods). Contrasting with recorded data, burst-rates increased linearly with bands' frequency ($BF_{10}>10^{31}$), whereas bands and category had no effect on burst duration ($BF_{01}=27.8$). Consequently, burst-rates in all transient bands of data were higher than their surrogate counterparts (Fig. 2A, blue vs. pink). In addition, burst-durations of beta1 and gamma1 were shorter than their surrogates. Conversely, burst-rates of the sustained bands alpha and beta2 were lower than simulated noise (Fig. 2A, green vs. pink), and the durations of alpha longer than expected by chance. Thus, low rhythmicity is associated with a high rate of transient oscillatory events, above and beyond what is expected from random $1/f$ activity.

But do bursts systematically affect rhythmicity? To address this, we simulated data and tested how manipulation of bursts' length affects rhythmicity levels. This *in-silico* approach revealed that bursts shorter than four cycles were associated with rhythmicity levels below what would be expected by chance, and hence can be considered transient (Fig. 2C). Conversely, bursts lasting more than 6 cycles were associated with rhythmicity levels significantly above chance, a characteristic of sustained activity. For these measures, we leveraged the defined threshold of our rhythmicity index. We simulated baseline neuronal activity as a signal with power in each frequency f weighted by $1/f$, and random phases. This signal's maximal and minimal rhythmicity values provided the baseline noise range. To mimic oscillatory bursts, we reduced the power in the 14-16 Hz range to $0.5/f$, and we increased it to $2/f$ for durations varying from 2 to 20 cycles (Fig. 2B). We obtained similar results with repeating rhythmic, but not arrhythmic, pulses (fig. S4) that can be mimicked experimentally with TMS. Therefore, we next turned to ask how single TMS pulses and repeating rhythmic and arrhythmic TMS pulses affect rhythmicity.

To causally demonstrate periodic input's role in rhythmicity, we stimulated six participants' prefrontal cortices with TMS (Fig. 2D). In line with the abovementioned computational modelling, we predicted that rhythmic stimulation should increase the rhythmicity measured in the scalp EEG, whereas arrhythmic stimulation might violate the phase consistency over time and thus disrupt ongoing oscillations. Furthermore, we predicted that single impulses should yield transient oscillations ("bursts" or "ripples") as their spectral fingerprint (*11*). Based on our hypothesis, these transient ripples should be confined to bands which naturally express burst dynamics. Our TMS approach indeed provided causal evidence that in low-rhythmicity bands transient activity is reverberated, whereas sustained bands are dominated by ongoing oscillations.

For each participant, we computed the rhythmicity profile at rest and determined their individual alpha, beta1 and beta2 peak frequencies. Then, for each band we stimulated 60 rhythmic trains of six pulses each with an inter-pulse-interval fixed to the cycle length of the peak frequency of this band. The arrhythmic condition also consisted of 60 trains of six pulses, with the same duration between the first and last pulse as in the rhythmic condition, but with random spacing between the remaining four pulses. In the last stimulation condition, we delivered a single pulse (120 trials, Fig. 2D). We pseudo-randomized the trial types' order (frequency band, rhythmicity, and whether a single or several pulses were delivered) and measured the stimulation's effect on rhythmicity at each time point using a time resolved phase locking measure (WTPL (*23*)).

Consistent with our hypothesis, single-pulse stimulations elicited reverberations in frequencies corresponding to the transient bands θ/α and beta1, that lasted up to 300 ms post-stimulation ($p<0.05$, cluster permutation test, Fig. 2E). Moreover, rhythmic pulses increased rhythmicity in all bands (Fig. 2F, peak frequency in each band marked as "0"). Arrhythmic stimulations, however, induced a band-rhythmicity-dependent effect. On the sustained bands alpha and beta2, arrhythmic stimulation caused a decrease in measured rhythmicity (significant (blue) clusters around peak frequency (0), Fig. 2G), implying that the arrhythmic stimuli disrupted ongoing oscillations. In beta1, arrhythmic stimulations had the opposite effect: they increased rhythmicity compared to baseline up to 200 ms after the last pulse, possibly due to the ripple induced in response to individual pulses. These results thus support our hypothesis that low-rhythmicity bands consist of transient yet spectrally defined activity, whereas high rhythmicity bands indicate sustained oscillations.

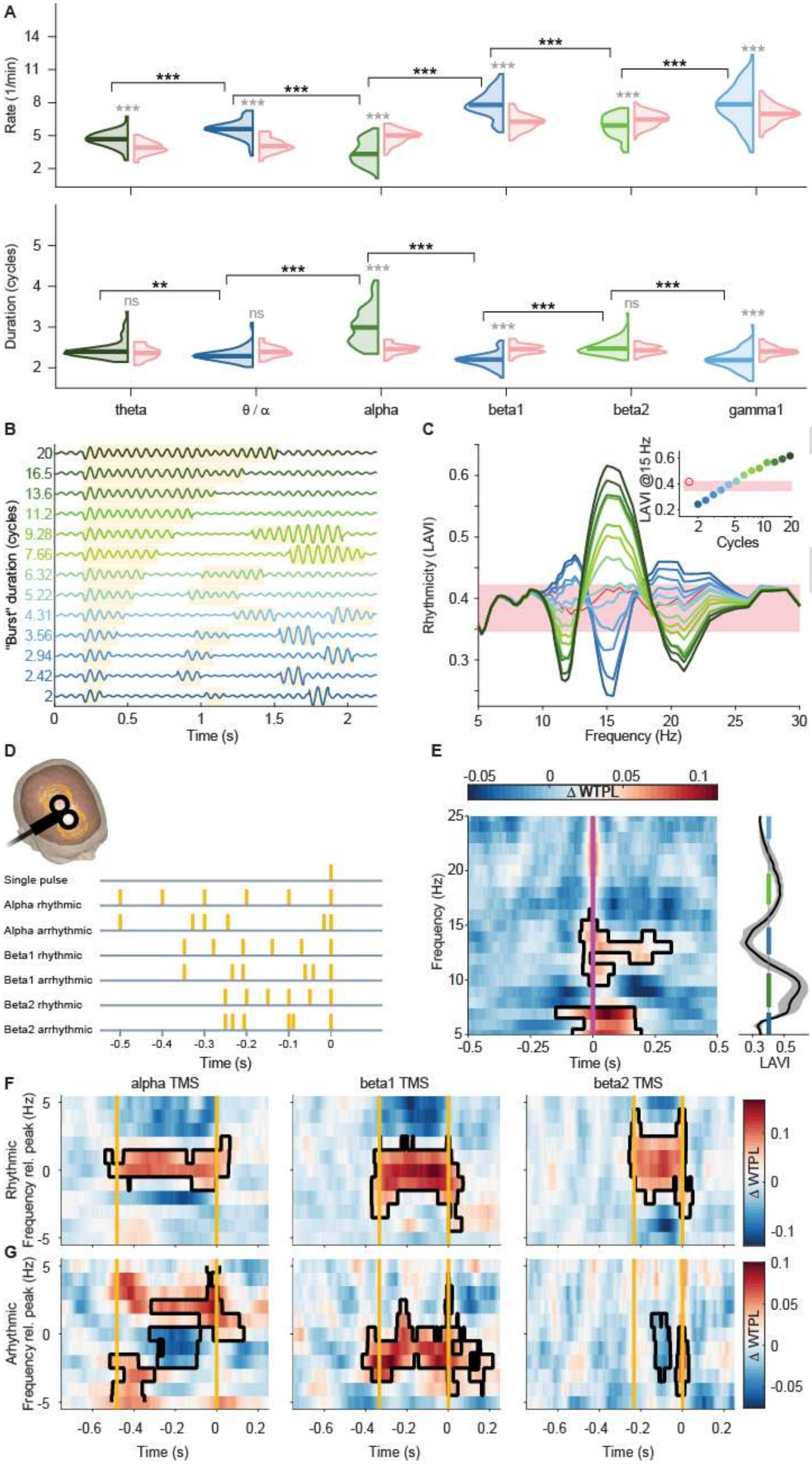

Figure 2. Rhythmicity is affected by oscillatory bursts.
(**A**) The rate (top row) and duration (bottom row) of oscillatory bursts in EEG data (N=90 participants, blue and green distributions, corresponding to bursty and sustained bands respectively) and simulations with participant-matched aperiodic 1/f noise (pink distributions). Violin plots represent the whole distribution, horizontal lines the median. **- $p<0.01$, ***- $p<0.001$, ns- not significant, ANOVA with Tukey's post-hoc. (**B**) Oscillatory bursts were simulated by filtering white noise with filters with a 1/f weight profile (thus generateing pink-noise), and setting the filter weight at the frequency of interest (15 Hz) to twice its original weight during burst (with varying length, ordinate), and half the weight elsewhere. Bursts are highlighted with gold background. (**C**) Rhythmicity profile. Colour of traces corresponds to burst length, pink shading corresponds to the noise, estimated as the minimal and maximal LAVI values of the 1/f-noise data (without adjustment, red trace). Inset: LAVI values at the modulated frequency (15 Hz). Note that increasing (decreasing) the rhythmicity in one band decreases (increases) rhythmicity in neighbouring bands. This can be caused by interference. However, peaks and troughs in physiological data are above and beyond this effect (for more details, see fig. S3). (**D**) TMS stimulations over rDLPFC alternated randomly between single pulses and trains of 6 Rhythmic or Arrhythmic stimulations (gold vertical lines). The specific frequencies of alpha, beta1 and beta2 were defined individually per participant, at rest (before stimulating). (**E**) Response to a transient (single-pulse) stimulation. Left: the within-trial phase-locking value (WTPL) at each frequency, normalized to a 0.5-1 s prestimulus baseline. Right: the average LAVI (n = 6 participants). Note increased WTPL values at LAVI troughs. (**F-G**) Response to rhythmic (**F**) and arrhythmic (**G**) repetitive stimulations. Gold vertical lines denote the first and last TMS pulses. Frequencies (ordinate) are relative to the individual peak frequency of each participant in each band. Black contour in (**B**) and (**C**): $p<0.01$ (cluster permutation).

Two modes of operation

Thus far, we introduced a spectral architecture incorporating both sustained and transient brain activity as universals. This framework is supported by data and enabled by our new methodology. Our hypothesis raises the possibility that this electrophysiological architecture serves a functional role. For example, this architecture may allow the brain to spectrally segregate two types of processes: change in response to inputs, manifested in oscillatory bursts which are transient, and maintenance of ongoing activity, reflected in sustained oscillations. Our fourth prediction therefore suggests that patterns of activity within the rhythmicity architecture should respond to cognitive states, and particularly those related to inputs. To demonstrate this, we exemplify how rhythmicity profiles and their relations with neuronal firing are affected by the amount of external input, both over the whole session and at the sub-second realm.

If activity in sustained bands entails maintenance of ongoing activity as opposed to response to input, then rhythmicity levels in these bands should decrease in the presence of sensory input. To examine this, we compared the rhythmicity profiles of healthy participants while performing a visual task relative to rest with their eyes closed (datasets I and II, Fig. 3A). Alpha-band power is known to decrease when people observe stimuli compared to wakeful rest with eyes closed (*34*). As theoretical anchoring, we confirmed that engaging in a task and being subjected to stimuli with eyes open also significantly decreases alpha-band rhythmicity ($p<0.01$, cluster-permutation test). Moreover, the difference in rhythmicity with eyes open compared to eyes closed (measured in LAVI) is highly correlated with the change in alpha power (measured in dB, $\rho=0.781$, $p<10^{-7}$). Furthermore, a significant increase in rhythmicity with eyes closed was observed also in the sustained band beta2 but was not observed in the transient band beta1. Notably, in addition to enabling the characterization of beta1 and beta2 as distinct modes of operation, this analysis points to the divergent roles of these modes.

We next asked what are the dynamics between neuronal firing and oscillations over the whole session, and how are they affected by visual inputs in the sub-second realm. If sustained band activity supports maintenance of ongoing processes, and transient band activity reflects response to change, then the relationship between oscillatory bands and neuronal firing should depend on the presence of external stimuli. Without inputs, we expect neuronal firing to correlate with activity in sustained bands. With inputs, however, neuronal firing should correlate with transient band activity. To investigate this, we turned to invasive recordings in humans, to enable measurement of the High-Frequency amplitude (HF, 70-150 Hz), a well-known proxy for neuronal firing (*29*). Using ECoG data from patients performing a visual perception task (dataset IX; Fig. 3B), we measured how the amplitude of HF activity covaries with the amplitude observed in each of the lower frequencies (LF, 3-45 Hz). Our framework predicts that as input processing increases, our HF proxy of neuronal activity should increasingly covary with transient band activity. We found that over the whole session, where in general the amount of input is low, HF significantly covaried with activity in sustained bands. In contrast, in response to a visual input, responding channels transiently increased their HF-LF covariance at a transient frequency band.

Specifically, the HF-LF covariance of all contacts over the entire session exhibited clear peaks at the sustained bands theta and beta2. When focusing on the time of visual stimulus presentation, however, we observed that HF-LF covariance differed between two subsets of channels. HF-activity clearly separates contacts that show increased HF following visual input versus those that show a decrease in HF (see (*29*) and supplementary material, materials and methods for further details). We consider the former as positively responding to the input and engaging in its processing (n=346 contacts), and the latter as negatively responding (n=84 contacts), potentially engaged in other, ongoing processes. Based on this interpretation, we predicted that positively responding contacts would exhibit stronger HF-LF covariation within transient bands upon stimulus presentation, reflecting their participation in input processing. In contrast, contacts that are inhibited by the stimulus would exhibit stronger HF-LF covariation within sustained oscillation bands, reflecting their involvement in computations other than the transient input. In line with these predictions, positively responding channels significantly increased their HF-LF covariance in the transient θ/α band (Fig. 3B, blue). Conversely, negatively responding channels significantly decreased their HF-LF covariance in the transient θ/α band and increased covariance in the sustained alpha band, supporting a role of alpha in inhibiting stimulus-unrelated regions (*35*). We note that the specific responding bands vary between tasks. This indicates that different transient and sustained bands can serve specific functional roles. Nonetheless, our exemplary invasive, non-invasive, and TMS stimulation data, suggest that typically, sustained bands (e.g., alpha, beta2) signify a mode of low engagement with external input, whereas transient bands (e.g., θ/α, beta1) represent engagement with incoming input.

Rhythmicity in health and disease

Finally, we tested whether rhythmicity may index variability between individuals, in health and disease. Rhythmicity as presented here can be robustly estimated at the individual participant level and compared against large sample data. For example, in healthy aging, peak frequencies and the range of the rhythmicity values decrease systematically (correlation between age and alpha frequency: Pearson's $\rho=-0.34$, $p<10^{-17}$, Fig. 1H; age and rhythmicity range: $\rho=-0.257$, $p<10^{-10}$, Fig. 3C). This neurotypical decline agrees with previous reports (*33*). Critically, this large-scale group characterization can serve as a norm for evaluating individuals' aging and diagnosing neurodegenerative diseases.

In addition, in Parkinson's disease (PD), beta power is known to increase. Activity in the low-beta band (12–24 Hz) is believed to be controlled by the level of dopaminergic activity in response to internal and external cues, and following dopaminergic cells' loss, beta levels are elevated in PD (*36*). This increase in beta amplitude in the subthalamic nucleus was found to correlate with beta-burst duration (*37*), and pathologically long beta-bursts are curtailed in response to medication (*38*). Therefore, we hypothesized that medication would specifically affect the transient-band beta1, and not the sustained band, beta2, of PD patients. We compared the rhythmicity profiles of PD patients with (i.e., "ON") and without (i.e., "OFF") medication, and found a significant increase specifically in beta1 in the "OFF" medication condition ($p<0.01$, cluster permutation test; Fig. 3D). This finding suggests that beta oscillopathy is specific to beta1 and demonstrates the importance of characterizing transient bands in spectral analysis. Future brain-stimulation treatments for PD and other diseases can thus benefit from improved functional resolution and band specificity, based on patients' individual rhythmicity profiles.

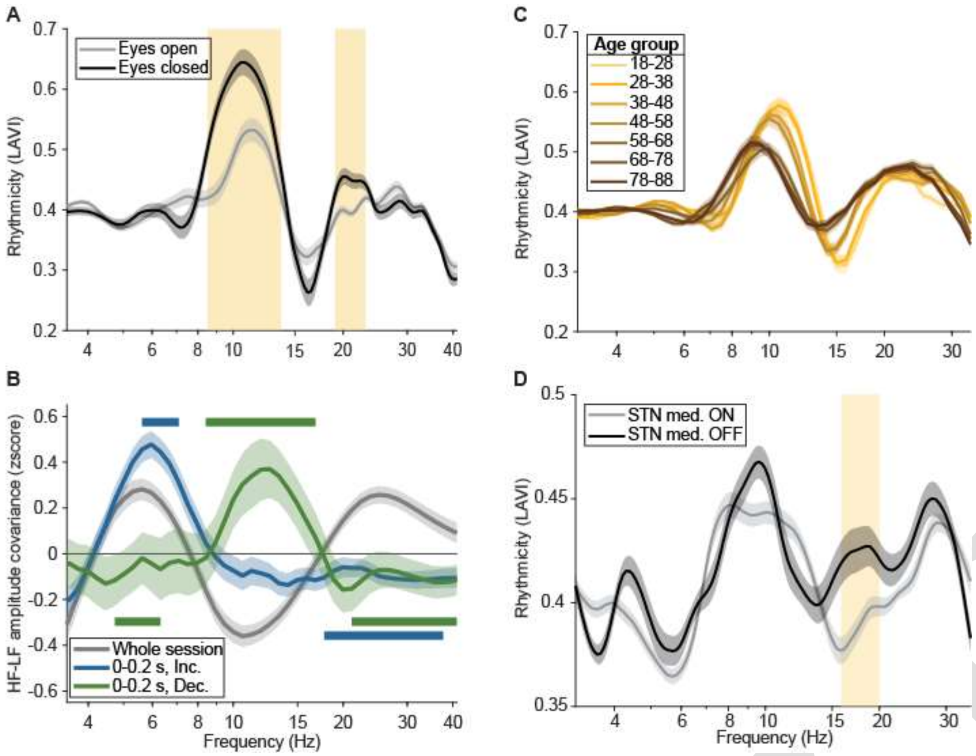

Figure 3. The functional effects of the rhythmicity architecture in health and disease.
In all panels, lines represent means and shaded areas the SEM. (**A**) The effect of openning eyes on rhythmicity. N=37, datasets I and II. Gold shades: $p<0.01$, cluster permutation. (**B**). Covariance between the amplitude of High-Frequency activity (HF, 70-150 Hz, a proxy of firing-rate) and the amplitude of activity in each of the Low-Frequencies (LF, x-axis) in dataset IX. Grey: calculated over the whole session and all channels. Blue: calculated at 0-0.2 s relative to a visual stimulus presentation, from channels showing increased HF in response to visual input (n=346 channels, 10 patients). Green: similar to blue, for channels showing decreased HF (n=84). Horizontal lines represent significant ($p<0.01$) difference between stimulation time to over-all-session. (**C**) The effect of healthy aging on rhythmicity (dataset VIII). N=625 participants. (**D**) The effect of L-Dopa medication on rhythmicity levels in the STN (dataset XI). N=30 hemispheres from 17 PD patients.

In conclusion, our findings offer a new perspective on the contribution of brain rhythms to information processing and cognition. We note that our experiments did not aim to resolve the debate about whether oscillations are *necessary* or *consequential* to neural computation (*39*). Nonetheless, based on our novel framework, which hinges on rhythmicity, we provide compelling evidence to settle the debate regarding the *involvement* of oscillations in neural computation. Rhythmicity-based spectral segmentation reveals twice as many bands as previously described with two divergent modes of operation. This indicates that there is room for both rate- and phase-codes with important complementary roles: activity in transient bands indicates neuronal inputs, whereas activity in high rhythmicity bands signifies maintenance of neuronal activity via sustained oscillations. This duality can conceivably expand the capacity and efficacy of neuronal computations and, with a spectrum spanning several orders of magnitude (*5*), can equip the brain with the flexibility necessary for a wide range of cognitive functions. The practical consequences of these theoretical insights are considerable; an individualized, detailed, and statistically robust spectral segmentation can be harnessed to develop brain-stimulation interventions and non-invasive neuropathological diagnostics, and to design novel brain-computer-interfaces.

References

1. G. Buzsáki, C. A. Anastassiou, C. Koch, The origin of extracellular fields and currents — EEG, ECoG, LFP and spikes. *Nat Rev Neurosci* **13**, 407–420 (2012).
2. G. Buzsáki, *Rhythms of the Brain* (Oxford University Press, New York, NY, US, 2006) vol. xv.
3. N. Kane, J. Acharya, S. Beniczky, L. Caboclo, S. Finnigan, P. W. Kaplan, H. Shibasaki, R. Pressler, M. J. A. M. van Putten, A revised glossary of terms most commonly used by clinical electroencephalographers and updated proposal for the report format of the EEG findings. Revision 2017. *Clin Neurophysiol Pract* **2**, 170–185 (2017).
4. E. Başar, B. Güntekin, A review of brain oscillations in cognitive disorders and the role of neurotransmitters. *Brain Research* **1235**, 172–193 (2008).
5. G. Buzsáki, A. Draguhn, Neuronal Oscillations in Cortical Networks. *Science* **304**, 1926–1929 (2004).
6. J. J. Newson, T. C. Thiagarajan, EEG Frequency Bands in Psychiatric Disorders: A Review of Resting State Studies. *Frontiers in Human Neuroscience* **12** (2019).
7. T. Donoghue, M. Haller, E. J. Peterson, P. Varma, P. Sebastian, R. Gao, T. Noto, A. H. Lara, J. D. Wallis, R. T. Knight, A. Shestyuk, B. Voytek, Parameterizing neural power spectra into periodic and aperiodic components. *Nat Neurosci* **23**, 1655–1665 (2020).
8. C. Han, T. Wang, Y. Yang, Y. Wu, Y. Li, W. Dai, Y. Zhang, B. Wang, G. Yang, Z. Cao, J. Kang, G. Wang, L. Li, H. Yu, C.-I. Yeh, D. Xing, Multiple gamma rhythms carry distinct spatial frequency information in primary visual cortex. *PLoS Biol* **19**, e3001466 (2021).
9. S. Nougaret, L. López-Galdo, E. Caytan, J. Poitreau, F. V. Barthélemy, B. E. Kilavik, Low and high beta rhythms have different motor cortical sources and distinct roles in movement control and spatiotemporal attention. *PLOS Biology* **22**, e3002670 (2024).
10. F. van Ede, A. J. Quinn, M. W. Woolrich, A. C. Nobre, Neural Oscillations: Sustained Rhythms or Transient Burst-Events? *Trends in Neurosciences* **41**, 415–417 (2018).
11. G. Karvat, M. Alyahyay, I. Diester, Spontaneous activity competes with externally evoked responses in sensory cortex. *PNAS* **118** (2021).
12. M. A. Sherman, S. Lee, R. Law, S. Haegens, C. A. Thorn, M. S. Hämäläinen, C. I. Moore, S. R. Jones, Neural mechanisms of transient neocortical beta rhythms: Converging evidence from humans, computational modeling, monkeys, and mice. *PNAS* **113**, E4885–E4894 (2016).

13. P. Fries, A mechanism for cognitive dynamics: neuronal communication through neuronal coherence. *Trends in Cognitive Sciences* **9**, 474–480 (2005).
14. P. R. Roelfsema, Solving the binding problem: Assemblies form when neurons enhance their firing rate—they don't need to oscillate or synchronize. *Neuron* **111**, 1003–1019 (2023).
15. M. A. Montemurro, M. J. Rasch, Y. Murayama, N. K. Logothetis, S. Panzeri, Phase-of-Firing Coding of Natural Visual Stimuli in Primary Visual Cortex. *Current Biology* **18**, 375–380 (2008).
16. P. Fries, D. Nikolić, W. Singer, The gamma cycle. *Trends in Neurosciences* **30**, 309–316 (2007).
17. W. A. Huang, Z. C. Zhou, I. M. Stitt, N. S. Ramasamy, S. Radtke-Schuller, F. Frohlich, Causal oscillations in the visual thalamo-cortical network in sustained attention in ferrets. *Current Biology* **0** (2024).
18. Y. Pan, T. Popov, S. Frisson, O. Jensen, Saccades are locked to the phase of alpha oscillations during natural reading. *PLOS Biology* **21**, e3001968 (2023).
19. J. O'Keefe, M. L. Recce, Phase relationship between hippocampal place units and the EEG theta rhythm. *Hippocampus* **3**, 317–330 (1993).
20. A. M. M. Fransen, F. van Ede, E. Maris, Identifying neuronal oscillations using rhythmicity. *NeuroImage* **118**, 256–267 (2015).
21. V. Myrov, F. Siebenhühner, J. J. Juvonen, G. Arnulfo, S. Palva, J. M. Palva, Rhythmicity of neuronal oscillations delineates their cortical and spectral architecture. *Commun Biol* **7**, 1–18 (2024).
22. H. Rayson, R. Debnath, S. Alavizadeh, N. Fox, P. F. Ferrari, J. J. Bonaiuto, Detection and analysis of cortical beta bursts in developmental EEG data. *Developmental Cognitive Neuroscience* **54**, 101069 (2022).
23. G. Karvat, N. Ofir, A. N. Landau, Sensory Drive Modifies Brain Dynamics and the Temporal Integration Window. *Journal of Cognitive Neuroscience* **36**, 614–631 (2024).
24. N. Ofir, A. N. Landau, Neural signatures of evidence accumulation in temporal decisions. *Current Biology* **32**, 4093-4100.e6 (2022).
25. Y. Noguchi, Individual differences in beta frequency correlate with the audio–visual fusion illusion. *Psychophysiology* **59**, e14041 (2022).
26. R. Hellerstedt, M. Johansson, M. C. Anderson, Tracking the intrusion of unwanted memories into awareness with event-related potentials. *Neuropsychologia* **89**, 510–523 (2016).
27. N. Legrand, O. Etard, F. Viader, P. Clochon, F. Doidy, F. Eustache, P. Gagnepain, Attentional capture mediates the emergence and suppression of intrusive memories. *iScience* **25**, 105516 (2022).
28. J. R. Taylor, N. Williams, R. Cusack, T. Auer, M. A. Shafto, M. Dixon, L. K. Tyler, Cam-CAN, R. N. Henson, The Cambridge Centre for Ageing and Neuroscience (Cam-CAN) data repository: Structural and functional MRI, MEG, and cognitive data from a cross-sectional adult lifespan sample. *NeuroImage* **144**, 262–269 (2017).
29. G. Vishne, E. M. Gerber, R. T. Knight, L. Y. Deouell, Distinct ventral stream and prefrontal cortex representational dynamics during sustained conscious visual perception. *Cell Reports* **42** (2023).
30. A. Barborica, I. Mindruta, V. J. López-Madrona, F.-X. Alario, A. Trébuchon, C. Donos, I. Oane, C. Pistol, F. Mihai, C. G. Bénar, Studying memory processes at different levels with simultaneous depth and surface EEG recordings. *Front. Hum. Neurosci.* **17** (2023).
31. C. Wiest, G. Tinkhauser, A. Pogosyan, M. Bange, M. Muthuraman, S. Groppa, F. Baig, A. Mostofi, E. A. Pereira, H. Tan, P. Brown, F. Torrecillos, Local field potential activity dynamics in response to deep brain stimulation of the subthalamic nucleus in Parkinson's disease. *Neurobiology of Disease* **143**, 105019 (2020).
32. K. Mizuseki, A. Sirota, E. Pastalkova, G. Buzsáki, Theta oscillations provide temporal windows for local circuit computation in the entorhinal-hippocampal loop. *Neuron* **64**, 267–280 (2009).
33. C. Babiloni, G. Binetti, A. Cassarino, G. Dal Forno, C. Del Percio, F. Ferreri, R. Ferri, G. Frisoni, S. Galderisi, K. Hirata, B. Lanuzza, C. Miniussi, A. Mucci, F. Nobili, G. Rodriguez, G. Luca Romani, P. M. Rossini, Sources of cortical rhythms in adults during physiological aging: A multicentric EEG study. *Human Brain Mapping* **27**, 162–172 (2006).
34. H. Berger, Über das Elektrenkephalogramm des Menschen. *Archiv f. Psychiatrie* **87**, 527–570 (1929).
35. M. Bonnefond, O. Jensen, Alpha Oscillations Serve to Protect Working Memory Maintenance against Anticipated Distracters. *Current Biology* **22**, 1969–1974 (2012).
36. S. Little, P. Brown, The functional role of beta oscillations in Parkinson's disease. *Parkinsonism & Related Disorders* **20**, S44–S48 (2014).
37. G. Tinkhauser, A. Pogosyan, S. Little, M. Beudel, D. M. Herz, H. Tan, P. Brown, The modulatory effect of adaptive deep brain stimulation on beta bursts in Parkinson's disease. *Brain* **140**, 1053–1067 (2017).
38. G. Tinkhauser, A. Pogosyan, H. Tan, D. M. Herz, A. A. Kühn, P. Brown, Beta burst dynamics in Parkinson's disease OFF and ON dopaminergic medication. *Brain* **140**, 2968–2981 (2017).
39. A. K. Engel, P. Fries, W. Singer, Dynamic predictions: Oscillations and synchrony in top–down processing. *Nat Rev Neurosci* **2**, 704–716 (2001).

Supplementary References

40. R. Oostenveld, P. Fries, E. Maris, J.-M. Schoffelen, FieldTrip: Open Source Software for Advanced Analysis of MEG, EEG, and Invasive Electrophysiological Data. *Intell. Neuroscience* **2011**, 1:1-1:9 (2011).
41. M. A. Shafto, L. K. Tyler, M. Dixon, J. R. Taylor, J. B. Rowe, R. Cusack, A. J. Calder, W. D. Marslen-Wilson, J. Duncan, T. Dalgleish, R. N. Henson, C. Brayne, F. E. Matthews, The Cambridge Centre for Ageing and Neuroscience (Cam-CAN) study protocol: a cross-sectional, lifespan, multidisciplinary examination of healthy cognitive ageing. *BMC Neurol* **14**, 204 (2014).
42. S. Taulu, J. Simola, Spatiotemporal signal space separation method for rejecting nearby interference in MEG measurements. *Phys. Med. Biol.* **51**, 1759 (2006).
43. V. Venema, F. Ament, C. Simmer, A Stochastic Iterative Amplitude Adjusted Fourier Transform algorithm with improved accuracy. *Nonlinear Processes in Geophysics* **13**, 321–328 (2006).

44. J. Theiler, S. Eubank, A. Longtin, B. Galdrikian, J. Doyne Farmer, Testing for nonlinearity in time series: the method of surrogate data. *Physica D: Nonlinear Phenomena* **58**, 77–94 (1992).

45. T. Schreiber, A. Schmitz, Improved Surrogate Data for Nonlinearity Tests. *Phys. Rev. Lett.* **77**, 635–638 (1996).

46. V. Venema, Surrogate time series and fields (2023). https://ch.mathworks.com/matlabcentral/fileexchange/4783-surrogate-time-series-and-fields.

47. G. Karvat, A. Schneider, M. Alyahyay, F. Steenbergen, M. Tangermann, I. Diester, Real-time detection of neural oscillation bursts allows behaviourally relevant neurofeedback. *Commun Biol* **3**, 1–10 (2020).

48. D. Apšvalka, C. S. Ferreira, T. W. Schmitz, J. B. Rowe, M. C. Anderson, Dynamic targeting enables domain-general inhibitory control over action and thought by the prefrontal cortex. *Nat Commun* **13**, 274 (2022).

49. S. Rossi, M. Hallett, P. M. Rossini, A. Pascual-Leone, Safety, ethical considerations, and application guidelines for the use of transcranial magnetic stimulation in clinical practice and research. *Clinical Neurophysiology* **120**, 2008–2039 (2009).

50. D. H. Brainard, The Psychophysics Toolbox. *Spatial Vision* **10**, 433–436 (1997).

51. N. C. Rogasch, C. Sullivan, R. H. Thomson, N. S. Rose, N. W. Bailey, P. B. Fitzgerald, F. Farzan, J. C. Hernandez-Pavon, Analysing concurrent transcranial magnetic stimulation and electroencephalographic data: A review and introduction to the open-source TESA software. *NeuroImage* **147**, 934–951 (2017).

52. E. Zmeykina, M. Mittner, W. Paulus, Z. Turi, Weak rTMS-induced electric fields produce neural entrainment in humans. *Sci Rep* **10**, 11994 (2020).

53. Y. Benjamini, Y. Hochberg, Controlling the False Discovery Rate: A Practical and Powerful Approach to Multiple Testing. *Journal of the Royal Statistical Society: Series B (Methodological)* **57**, 289–300 (1995).

54. B. Krekelberg, BayesFactor: Release 2022 (v2.3.0), version v2.3.0, Zenodo (2022); https://doi.org/10.5281/zenodo.7006300.

55. J. van Doorn, D. van den Bergh, U. Böhm, F. Dablander, K. Derks, T. Draws, A. Etz, N. J. Evans, Q. F. Gronau, J. M. Haaf, M. Hinne, Š. Kucharský, A. Ly, M. Marsman, D. Matzke, A. R. K. N. Gupta, A. Sarafoglou, A. Stefan, J. G. Voelkel, E.-J. Wagenmakers, The JASP guidelines for conducting and reporting a Bayesian analysis. *Psychon Bull Rev* **28**, 813–826 (2021).

56. E. Maris, R. Oostenveld, Nonparametric statistical testing of EEG- and MEG-data. *Journal of Neuroscience Methods* **164**, 177–190 (2007).

57. E. M. Gerber, permutest, *MATLAB Central File Exchange* (2023). https://www.mathworks.com/matlabcentral/fileexchange/71737-permutest.

Acknowledgments

We thank Profs. Rik Henson and Leon Deouell for insightful comments as well as data use. We also thank Flor Kusnir, Nir Ofir, Anna Goodman, and Yarden Weiss, for providing helpful remarks on previous drafts of this article.

Funding:

German Research Foundation Walter-Benjamin post-doctoral fellowship KA 5804/1-1 (GK)
Azrieli Foundation graduate fellowship (GV)
Edmond and Lily Safra Center fellowship for Brain Sciences graduates (GV)
Medical Research Council grant MC-A060-5PR00 (MCA)
James McDonnell Scholar Award in Understanding Human Cognition (ANL)
ISF grant 958/16 (ANL)
European Research Council (ERC) under the European Union's Horizon 2020 research and innovation programme 852387 (ANL)

Author contributions:

Conceptualization: GK

Data curation: GK, GV

Formal analysis: GK, MCG, GV

Funding acquisition: GK, MCA, ANL

Investigation: GK, MCG

Methodology: GK, ANL

Project administration: GK, MCA, ANL

Resources: MCA, ANL

Software: GK, MCG, GV

Supervision: MCA, ANL

Visualization: GK, ANL

Writing – original draft: GK, MCA, ANL

Writing – review & editing: GK, MCA, ANL

Competing interests

Authors declare that they have no competing interests.

Data and materials availability:

A Matlab implementation for LAVI and ABBA (including pink surrogate and look-up table generation) is available at https://github.com/laaanchic/LAVI.

The raw data of each dataset used in this study are available at:

I, II, and III: requests for data should be directed to and will be fulfilled by ANL (ayelet.landau@mail.huji.ac.il).

IV: https://dataverse.harvard.edu/dataset.xhtml?persistentId=doi:10.7910/DVN/YD7PPU

V: requests for data should be directed to and will be fulfilled by the corresponding authors of ref. *26*, Mikael Johansson (mikael.johansson@psy.lu.se) and Robin Hellerstedt (robin.hellerstedt@ctb.upm.es).

VI: further information and requests should be directed to and will be fulfilled by the lead contact of ref. *27*, Pierre Gagnepain (pierre.gagnepain@inserm.fr).

VII: https://figshare.com/articles/dataset/EEG_at_rest_and_with_TMS/27934962/2

VIII: https://camcan-archive.mrc-cbu.cam.ac.uk/dataaccess/

IX: https://osf.io/4hxpw/

X: http://epi.fizica.unibuc.ro/scalesoldnew/

XI: https://data.mrc.ox.ac.uk/stn-lfp-on-off-and-dbs

XII: https://portal.nersc.gov/project/crcns/download/hc-3

Supplementary Materials

Materials and Methods.

Supplementary Text.

Figs. S1 to S5.

References 40-57 are only cited in the Supplementary Materials.

Supplementary Materials for

Universal rhythmic architecture uncovers distinct modes of neural dynamics

Golan Karvat, Maité Crespo-García, Gal Vishne, Michael C Anderson, Ayelet N Landau

Corresponding author: golan.karvat@mrc-cbu.cam.ac.uk

Materials and Methods

Participants and data acquisition

We sought to establish the rhythmicity architecture as a universal phenomenon, therefore we analyzed datasets from different laboratories and recording techniques. Details of the original publications from which data were analysed in this study is presented in the main text, Table 1.

EEG acquisition and preprocessing

We performed all offline preprocessing and analysis steps using the Fieldtrip toolbox, release 20230822 (*40*) and custom code in Matlab 2020b (MathWorks, Natick, MA). In datasets I-III (*23*, *24*), data were sampled at 512 Hz using a g.GAMMAcap (gTec, Schiedlberg, Austria) and a g.HIamp amplifier (gTec). The cap had 62 electrodes distributed over the scalp, with the addition of two active earlobe electrodes. All electrodes were re-referenced offline to the average of the earlobe electrodes. In dataset IV (*25*), data were sampled at 2048 Hz using an ActiveTwo EEG system (Biosemi, Amsterdam, Netherlands). The cap had 32 electrodes that were re-referenced offline to the average of two electrodes over the temporal lobe (T7 and T8)[1]. Data in dataset V (*26*) was recorded with a Neuroscan (Compumedics, El Paso, TX, USA) NuAmps amplifier, with 30 channels sampled at 1000 Hz and re-referenced to electrodes over he left and the right mastoid. In dataset VI (*27*), data were acquired from 128 channels using EGI Hydrocel Geodesic Sensor Net (HGSN-128, Magstim EGI, Eugene, OR), sampled at 1000 Hz, and re-referenced offline to the average of all channels.

All succeeding preprocessing procedures were identical for all EEG datasets. We detrended, demeaned and bandpass filtered the data at 0.5-130 Hz. Then, we inspected the data visually and rejected bad channels, inserting interpolation of neighbouring channels instead of the bad channels. On average, we rejected 8.54% of electrodes from dataset I (SD 1.65%), 0.04% (0.26%) from dataset II, 2.3% (3.2%) from dataset III, 1.17% (2.22%) from dataset IV, 4.5% (1.9%) from dataset V, and 5.9% (5.0%) from dataset VI. Importantly, channel Cz, which was used for rhythmicity and oscillatory bursts analyses in Fig. 1, Fig. 2, and Fig. 4, was good for all 178 EEG subjects. Scalp muscle artefacts were detected and marked as epochs in which the amplitude of the signal at 100-120 Hz at all channels exceeded a threshold of 30 standard deviations. Finally, independent spatio-temporal components containing eye movements (blinks and saccades) were removed using independent component analysis (ICA). We preformed all preprocessing steps, as well as rhythmicity (LAVI), power, and oscillatory bursts analyses, on the whole session (that is, without dividing into trials).

---

[1] As recommended for channel level analysis when earlobe electrodes are unavailable, see https://www.fieldtriptoolbox.org/getting_started/biosemi/

For ECoG (dataset IX) we used all 907 channels reported "clean" in the original publication (*29*). In the per-area analysis (Fig. 1I) we excluded electrodes reported as "Medial" due to low count (n=12), or those lacking anatomical localization (n=28). After exclusion, this analysis consisted of 867 electrodes. For SEEG (dataset X (*30*)) we used 733 electrodes reported as located in mesial-frontal, lateral-frontal, insula, medial-parietal, lateral-parietal, lateral-temporal, or mesial-temporal areas. In addition, for each area, we included the nearest concurrently recorded EEG scalp electrode. For LFP recordings, we used one STN channel from each hemisphere On and Off PD medication in dataset XI (*31*) sampled at 2048 Hz using a TMSi Porti (TMS International, Netherlands) or from the hippocampus of each rat in dataset XII (*32*).

MEG acquisition and preprocessing

MEG data came from Stage 2 of the Cambridge Centre Aging and Neuroscience (Cam-CAN; www.cam-can.org; (*41*)) study of healthy adult ageing (aged 18-88 years). Ethical approval was obtained from the East of England-Cambridge Central Research Ethics Committee, and participants gave full informed consent. A detailed description of exclusion criteria can be found in (*41*), Table 1. Of these, only participants with resting state MEG data that could be corrected for motion using MaxFilter were used here (n = 625).

MEG data were collected using a 306-channel VectorView MEG system (Elekta Neuromag, Helsinki), consisting of 102 magnetometers and 204 orthogonal planar gradiometers, located in a magnetically shielded room. MEG resting state data (sampled at 1 kHz with a high-pass filter of 0.03 Hz) were recorded approximately 8.5 mins, while participants remained still in a seated position with their eyes closed, but instructed to stay awake. Head position within the MEG helmet was estimated continuously using four Head-Position Indicator (HPI) coils to allow offline correction of head motion.

The MaxFilter 2.2.12 software (Elekta Neuromag Oy, Helsinki, Finland) was used to apply temporal signal space separation (*42*) to the continuous MEG data to remove noise from external sources (correlation threshold 0.98, 10-sec sliding window), to continuously correct for head-motion (in 200-ms time windows), to remove mains-frequency noise (50-Hz notch filter), and to detect and reconstruct noisy channels. Following these de-noising steps, data were imported into Matlab using SPM12 (http://www.fil.ion.ucl.ac.uk/spm). These data are available on request from https://cam-can.mrc-cbu.cam.ac.uk/dataset/.

The first 20 seconds of data were ignored to allow participants to settle, and any samples after 542 seconds were ignored, in order to match data length across participants (to the minimum duration across participants). These data were then extracted from 4 magnetometers around Cz.

Lagged Angle Vector Index (LAVI)

We measured rhythmicity as the consistency of the relations of phase (angle) between data points that are separated by a fixed time interval (lag). The rational for defining rhythmicity in this manner is that the phase of a sustained oscillation at any time-point should predict its future phase (*20*).

We computed the time-frequency representation $\hat{x}$ for each time-point t and frequency of interest f using complex Morlet wavelets, of the form

$$w(t,f) = Ae^{\left(\frac{-2(\pi f t)^2}{m^2}\right)} e^{(2i\pi f\ )}$$

where i is the imaginary unit and m is the wavelet width, measured in cycles. The normalization factor was $A = \sqrt{2f\sqrt{\pi}/m}$. The value of m was set to 5, based on the exploration presented in fig. S2D. A care was taken to produce angles with convention: cosine must always be 1 and sine must always be cantered in upgoing flank, so the centre of the wavelet has angle = 0 rad (*40*). The time frequency representation was calculated by multiplying the Fourier transforms of the data and the wavelet of each frequency, and taking the inverse transform of the product. Then, the rhythmicity λ was measured for each frequency as the magnitude of the vector mean vector of all angle differences ("coherence") between the original time-frequency representation $\hat{x}_{(t,f)}$ and a copy of itself with a constant lag of τ cycles $\hat{x}_{(t+L_{(f)},f)}$:

$$\lambda(f) = \left| \frac{\sum_{t=1}^{T-L_{(f)}} \hat{x}_{(t,f)} \hat{x}'_{(t+L_{(f)},f)}}{\sqrt{\left(\sum_{t=1}^{T-L_{(f)}} \left|\hat{x}_{(t,f)}\right|^2\right)\left(\sum_{t=1}^{T-L_{(f)}} \left|\hat{x}_{(t+L_{(f)},f)}\right|^2\right)}} \right|$$

where *T* is total number of time points in the session, $L_{(f)}$ is the number of time points in τ cycles and the superscript $'$ denotes the complex conjugate transpose. By definition, λ assumes values between 0 and 1. The median of λ (over *f*) is stable across subjects and depends on *m* and τ. Based on the exploration presented in fig. S2D, we set τ to 1.5 cycles, which together with *m* = 5 cycles yields a median λ of ~0.4, providing a good dynamic range (for further discussion, see Supplementary Text, Parametrical effects on rhythmicity measures, below).

Automated Band Border Algorithm (ABBA)

Using the LAVI median as a threshold, one can define areas above the median as "sustained" bands, and areas below as "transient" bands. However, fluctuations above and below the median are present also in the rhythmicity profiles of purely random signals (noise). The median of the rhythmicity profiles of noise also depends of *m* and τ, and their dispersion range depends on the sampling frequency, session duration, and the aperiodic slope (for further discussion, see Supplementary Text, parametrical effects on rhythmicity, and fig. S5). This relationship can be leveraged to determine spectral bands with statistical confidence using bootstrap: frequencies with a rhythmicity level above (below) the distribution of *n* instantiations of noise, can be considered sustained (transient) with type I error α = 1/*n*.

To generate the distribution of rhythmicity profiles we generated surrogates that matched the aperiodic component (1/*f*) of each subject. We calculated the aperiodic component of the EEG by fitting an exponential function to the EEG power spectrum, and used the fitted values as the input for an Iterative Amplitude Adjusted Fourier Transform algorithm (IAAFT, (*43–45*)). IAAFT generates surrogate time series with a desired power spectrum (in the frequency domain) and data values (in the time domain) by keeping the original magnitude of the Fourier coefficients and assigning random phases. In each iteration of the algorithm there are five steps: a. shuffling the data; b. calculating the Fourier transform of the shuffled data; c. replacing the magnitudes of the shuffled Fourier spectrum with the desired magnitudes; d. calculating the adapted time series using inverse Fourier transform, and e. assigning the values of the original data to the adjusted time-series based on ranking (the highest value of the surrogate gets the highest value of the original data and so forth). Since the last step can change the power spectrum, both the amplitude and the spectral adjustments are repeated iteratively until the difference between the desired and adapted spectra subceeds a threshold (here, we used a threshold of $2*10^{-4}$ of the standard deviation of the original data).

For each subject, we generated 20 surrogate instantiations using an implementation for Matlab of the IAAFT (*46*). The IAAFT can take the original EEG values as input, but in order to be robust to artifacts, we used random data with a range equal to the central 99% of the EEG as input to the IAAFT algorithm. We calculated the rhythmicity profile of each instantiation, and used the highest and lowest LAVI values (over all frequencies and instantiations) as the significance limits with α = 0.05 (1/20). Then, ABBA defines each frequency with a LAVI value above (below) the significance limit as significantly sustained (transient). Frequencies between points of crossing the median are then grouped into bands. The local maximum is taken as the peak frequency of sustained bands, and the local minimum is the peak frequency of transient bands. Since most subjects have a clear peak in the rhythmicity profile at the alpha band, the peak between 6 to 14 Hz can be used as an anchor to automatically allocate bands identity: the frequency with highest rhythmicity between 6 and 14 Hz is taken as alpha, the trough to the right of alpha is beta1, the next peak is beta2, and so forth, and also for frequencies lower than alpha. A Matlab implementation for LAVI and ABBA (including pink surrogate and look-up table generation) is available at https://github.com/laaanchic/LAVI. This code is using functions provided by Fieldtrip (*40*) and Venema V. (*46*), and is shared under the GNU General Public License (GPL) and Berkeley Software Distribution (BSD) license, respectively.

In fig. S2 we compare band-detection with LAVI and ABBA to a commonly used power-based method. To this end, we computed the power spectrum of the EEG of 90 participants (using the Matlab function 'pwelch'), and used Spectral parameterization (specparam, formerly fooof (*7*)) with recommended default configurations to detect the range and peak frequency of bands.

Simulations

For all simulations presented in Figs. 2, 3, S1, S4, and S6, we generated 180 s "pink" surrogate data using IAAFT, with aperiodic exponent of -1, range of ~100 µV, mean 0µV and SD ~12.5 µV. In order to manipulate the activity in a specific frequency, we decomposed the signal using an array of Butterworth bandpass filters (order = 3), centred at frequencies 3 to 100 Hz in steps of 1 Hz and bandwidth of 1 Hz, manipulated the activity in 15 Hz, and then recomposed the signal by summation of the filtered data. After each manipulation iteration, we calculated and stored the rhythmicity profile (LAVI).

To manipulate "burst" durations (Fig. 2), we first "notch filtered" the activity in 14-16 Hz by multiplying the filtered signal at this frequency by 0.5. Then, we set the values during "bursts" as twice the original value, with a smooth rise and fall. The duration of each "burst" was the independent variable and ranged logarithmically between 2 and 20 cycles, and the duration between "bursts" jittered between 5 and 15 cycles.

In the transient input simulations (fig. S4), the initial conditions were identical to the oscillatory burst duration simulation. Each transient input was simulated as an impulse (one sample long) with amplitude equal to the EEG range (100 µV). The number of impulses in a "burst" was the independent variable and ranged linearly from 1 to 13. In the rhythmic condition (fig. S4A-B), the distance between each impulse in a "burst" was set to 66.6 ms (one cycle of a 15 Hz oscillation). In the arrhythmic condition (fig. S4C-D), the last impulse in a "burst" was set to 66.6*(n-1) ms after the first pulse, with n the number of impulses in a "burst". Then, the remaining n-2 impulses were randomly distributed between the first impulse and last impulse. Like in the burst duration simulation, the inter "burst" interval jittered between 5 and 15 cycles.

To implement phase shifts (fig. S1), we flipped the sign of the signal by multiplying it by -1 every 2 to 20 cycles (in logarithmic steps). To investigate the effect of power on rhythmicity (fig. S3A-B), we multiplied the data filtered at 15 Hz by values ranging between 0.1 and 2, in steps of 0.1. In all simulations, we defined the significance limits as the maximum and minimum rhythmicity values of the original surrogate data, and the main dependent variables were the rhythmicity values at the manipulated frequency (15 Hz). All rhythmicity calculations were made with Wavelet width of 5 cycles and lag of 1.5 cycles.

To investigate if the troughs in the rhythmicity profiles we observed in the data of 90 subjects can be explained as an (artefactual) effect of the peak in alpha, we generated 90 instantiations of 120 s 1/f surrogates. We decomposed the surrogates into discrete frequencies, and multiplied the amplitude of the signal in 11 Hz (alpha) by a factor randomly chosen between 1.05 and 2.25. We then calculated the rhythmicity profiles (LAVI) and detected bands (ABBA). Then, we calculated the fit between the LAVI values at alpha peak and beta1 trough of the surrogate population with a linear regression. We used the coefficients of the regression to calculate the expected beta1 troughs based on data alpha peaks, and compared them to beta1 troughs observed in data (fig. S3C-D). Finally, we compared the LAVI values at theta/ alpha and beta1 troughs of the data to the troughs of surrogates generated with aperiodic components and power in alpha matching the observed data, using filter arrays (fig. S3E).

Bursts detection

To detect oscillatory bursts, we first estimated the power of the raw EEG using Morlet wavelets with width of 5 cycles, centered at frequencies ranging from 3 to 42 Hz in steps of 1 Hz. Then, we removed artefactual segments defined as timestamps in which the EEG exceeded 250μV or durations marked as muscle artefacts during preprocessing, and 500 ms before and after them (*47*). A burst peak time and frequency were defined as regional maxima in the 2D (time x frequency) plane, that also exceeded the 90th power percentile. For each peak we documented the peak frequency, maxima timing, and the beginning and end time (defined as points in which the power in the peak frequency dropped below the 75th percentile). Since we were interested in average durations and rates of bursts in the different bands over the whole session, we paid special attention to avoid bursts overlapping in time/ frequency. Therefore, if two bursts overlapped in time, and also had peak frequencies difference smaller than a quarter of the peak frequency of any of the bursts, they were merged into one burst. The merged burst assumed the frequency of the burst with the higher energy (estimated as power x duration).

TMS- procedure

All procedures were approved by the Cambridge Psychology Research Ethics Committee. All participants provided written informed consent prior to data acquisition for the study. Biphasic single and repetitive TMS pulses were delivered using a DuoMAG XT-100 TMS stimulator and a figure-of-eight coil DuoMAG 70BF (Brainbox Ltd, Cardiff, UK). During the stimulation, participants sat in a comfortable recliner chair with a neck rest. To ensure the precise targeting of specific brain regions, the coil was controlled via Brainsight 2 neuronavigation system (Brainbox) in combination with an Axilum TMS-Cobot (Axilum Robotics, Schiltigheim, France). The Cobot is a robotic system that actively monitors and adjusts the positioning of the coil, and compensates for head movements throughout the experiment. To detect head movements, participants wore a headband reference tracker that was monitored by a Polaris Vega ST camera (NDI, Waterloo, Canada). The TMS coil was oriented with the handle pointing posteriorly with respect to the participant's head, at an angle of 45 degrees relative to midline. The MNI coordinates for dorso-lateral prefrontal cortex (dlPFC, x = 33, y = 39, z = 26) stimulation were derived from the peak voxel showing the strongest effect in BOLD signal in a previous meta-analysis study (*48*).

Our protocol established a TMS stimulation intensity at 90% of the resting motor threshold (RMT) of each participant. To determine the RMT, we positioned the coil over the hand area of the right primary motor cortex and asked the participant to keep their left hand relaxed and at rest. Then, we determined the minimum intensity at which a single TMS pulse produced a visible twitch in the abductor pollicis brevis muscle of their left hand, in five of ten successive pulses.

EEG recordings were obtained with the actiCHamp Plus 64 system (Brain Products GmbH, Gilching, Germany), which is TMS-compatible. The system includes a DC-coupled amplifier avoiding AC recoding and high-pass filter during the recording period. EEG signals were acquired from 64 active electrodes arranged on an actiCAP slim electrode cap. The ground electrode was placed at FPz, and the reference at Cz. Electrode impedance was maintained below 20 kOhm. We used a sampling rate of 1000 Hz for the EEG resting-state recording and 5 kHz or the TMS-EEG recordings.

After EEG setup, we used LAVI and ABBA to determine the individual alpha, beta1, and beta2 peak frequencies that would define the repetitive TMS stimulation frequencies. For this, we performed a resting-state EEG recording of 12 minutes (2-minutes with open eyes, 8-minutes closed eyes, and 2-minutes open eyes). During the fixation periods, participants were instructed to keep their eyes still and look at a white fixation cross presented on a black background. The open-eyes EEG recordings were quickly pre-processed with a Matlab script. LAVI was calculated over the closed-eyes period.

The TMS-EEG session comprised a total of 480 trials distributed into 8 blocks. There were 7 conditions: single pulse (sp-TMS), 3 rhythmic conditions consisting of a 6-pulses train at alpha, beta1 or beta2 individual frequencies, and 3 arrhythmic conditions, also consisting of 6-pulses train. For each arrhythmic condition we precomputed patterns of 6-pulses that excluded frequencies within a +/-2-Hz band centred on the frequency of the corresponding rhythmic condition, their harmonics, subharmonics and over 50 Hz. The length of both rhythmic stimuli was equal to 5 cycles of the peak frequency. Each block included 12 trials of the single pulse condition and 8 trials of each of the rhythmic and arrhythmic conditions, presented sequentially in a pseudorandomized order. During each block, participants were instructed to keep their eyes still and look at a white fixation cross presented on a black background. The inter-train interval (ITI) between two consecutive trials was adjusted to the preceding frequency according to safety guidelines (*49*). For frequencies up to 10 Hz, we used a 3-s ITI; for frequencies over 10 Hz and up to 15 Hz, we used a 5-s ITI; for frequencies over 15 Hz and up to 20 Hz, we used an 8-s ITI; for frequencies over 20 Hz and up to 25 Hz, we used a 10-s ITI. Stimulus and TMS pulses delivery was controlled using Psychtoolbox-3 (*50*) in Matlab.

TMS- data analysis

EEG data were pre-processed offline in Matlab using Fieldtrip and custom-written code, following previously published guidelines (*51*, *52*). First, we removed the TMS ringing artefacts by replacing data values from 1 ms before to 15 ms after the TMS pulse trigger with NaNs (Not-a-Number). Then, we down-sampled the data to 1000 Hz. Afterwards, we visually inspected the data and marked fragments with major artefacts (e.g., jumps, movement, muscle); these fragments were also replaced by NaNs. Then, all the fragments with NaNs were interpolated with a linear method. To detect remaining TMS-related artefacts, we ran a first independent component analysis (ICA) with the FastICA algorithm. We averaged the components' signal 50 ms after TMS pulse over all trials and rejected those components whose amplitude exceeded 30 µV. Then, we ran a second ICA. In this run, components relating to eye blinks, eye movements, muscle and sensor-localized noise were identified and removed. All bad data fragments were replaced via Piecewise Cubic Hermite Interpolation (pchip). Then, the Cz reference channel was recovered and the data was re-referenced to a common average reference. Finally, the data were cut into segments of each trial type, including a pre-train onset interval of 2.5 sec and post-train offset interval of 2 sec.

Time-resolved rhythmicity

To measure how rhythmicity changes in time within a trial in response to TMS (Fig. 2E-G), we used the Within Trial Phase Lock (WTPL) method. This method is described in detail elsewhere (*23*). In brief, WTPL measures time-resolved rhythmicity by asking how sustained the oscillation is for at least one period (5, 11). In each frequency of interest, time-point, and trial, we computed the difference between the phase in the time-point of interest (ϕ_0), one cycle beforehand (ϕ_{-1}) and one cycle after (ϕ_1). The WTPL is computed as the mean resultant vector length of the two differences:

$$WTPL(f,t,n) = \frac{1}{2}\left|e^{i(\phi_0-\phi_1)} + e^{i(\phi_0-\phi_{-1})}\right|$$

with f stands for frequency, *t*- time, and *n*- trial. A Matlab implementation for WTPL is available at https://github.com/laaanchic/WTPL.

Note that since baseline levels of certain frequencies are higher than others (as learned from LAVI), between-frequency analysis is done after baseline subtraction (termed ΔWTPL in Fig. 2). We took the duration -1 s to -0.5

s (relative to the first TMS impulse) as baseline. Note, that the TMS frequency used for each participant was dependent on their individual band peak frequency, which varied across participants. Therefore, in Fig. 2, we plotted the population-averaged ΔWTPL values after normalizing individual frequencies (that is, setting the peak frequency per band to "0").

Amplitude covariance

We used the High-Frequency (HF) activity estimation and separation of electrodes into positively and negatively responding to the visual stimuli as reported in (*29*). To estimate HF, the entire signal was band-pass filtered into eight 10 Hz sub-ranges between 70 and 150 Hz. Then, instantaneous amplitude in each band was extracted using the Hilbert transform. To account for the $1/f$ profile of the power spectrum, the amplitude in each sub-range was normalized by dividing the instantaneous amplitude by the mean amplitude in that range. Finally, the amplitude traces from all sub-bands was averaged. Channels were defined as responsive if the HF activity in one of four non-overlapping "stimulus-on" windows (0.1-0.3 s, 0.3-0.5 s, 0.5-0.7 s, and 0.7-0.9 s relative to stimulus onset) differed significantly from baseline activity (-0.2-0 s) for at least one of the four categories of visual stimuli used in the study (faces, watches, objects, and animals). Trials containing excessive noise at -0.3 to 1.6 s relative to stimulus onset, or with stimulus duration shorter than 900 ms, were excluded from analysis. For each category, the mean HF signal during the "stimulus-on" window was compared to the mean HF during baseline (two-tailed paired *t*-test with Benjamini-Hochberg False discovery rate correction (*53*) between electrodes and Bonferroni correction between windows). Hence, electrodes with qFDR < 0.05/4 in at least one of the four windows were considered responsive. Electrodes were considered "positively responsive" if activity during the "stimulus-on" window increased relative to baseline, and "negatively responsive" when it decreased.

To estimate the Low-Frequency (LF) activity, we computed the time-frequency representation of the raw data using complex Morlet wavelets. The wavelets were centered on frequencies spanning logarithmically the range 3 to 45 Hz, with width of 5 cycles each. To extract the amplitude, we took the complex magnitude (absolute value) of the complex wavelet output. We then computed for each electrode and each Low-Frequency the covariance between the LF amplitude and normalized (*z*-transformed across time) HF and activities. This normalization was performed to account for differences in HF activity between electrodes. We calculated the covariance over the whole session (grey trace in Fig. 3B) or in response to the visual stimulus onset (0-0.2s, blue and green traces in Fig. 3B).

Statistical tests

All statistical tests were performed using Matlab with the Statistics and Machine Learning toolboxes. Data throughout this manuscript are presented as mean ± *SEM* unless otherwise stated. Significance level was set at $\alpha = 0.05$. To define bands with statistically significant increased or decreased rhythmicity we adopted a bootstrap approach. For each participant in datasets I-VIII we simulated 20 instances of surrogate data that matched the duration, sampling frequency, and aperiodic exponent of the original data, but with random phases. We used the IAAFT algorithm (*43–45*) to generate these surrogates. Then, we calculated the LAVI of each surrogate, yielding a distribution of 20 "noise ribbon" LAVI values per frequency. The maximal and minimal values per frequency were taken as significance limits. Thus, frequencies in the original data with LAVI values higher than the maximal value of the surrogate distribution were defined as having significantly (p=1/20=0.05) high rhythmicity. Similarly, real-data frequencies with lower LAVI values than the surrogate distribution were defined as having a significantly low rhythmicity. To facilitate the computation of hundreds of channels, we generated surrogate distributions with different sampling frequencies, durations, and aperiodic exponents. This resulted in a look-up table that was used to define significance limits for each channel in datasets ix-xii.

To test for differences in band-peak distributions between datasets, age groups, or areas (Fig. 1 G-J), as well as for differences in burst characteristics between bands (Fig. 2A), we used a one-way ANOVA (Matlab function "anova1"), followed by Tukey's honest significant difference post-hoc tests. To test whether or not a difference in band-peak distribution exists between deep-electrodes and the nearest scalp-EEG (Fig. 1K) or between hippocampal recordings in humans and rats (Fig. 1L) we used Bayes Factor (BF) t-tests, using a BF toolbox for Matlab (*54*). The output of the bf.ttest Matlab function is BF_{10}, or how strong is the evidence to support H_1 (the distributions are different) and reject H_0 (the distribution are not different). To determine the strength of this evidence we followed the guidelines suggested in (*55*): $3<BF_{10}<10$ indicates a moderate evidence for H_1, and $BF_{10}>10$ indicates a strong evidence for H_1. Similarly, $1/10<BF_{10}<1/3$ (or $3<BF_{01}<10$, where $BF_{01}=1/BF_{10}$) indicates a moderate evidence for H_0, and $BF_{10}<1/10$ (or $BF_{01}>10$) indicates a strong evidence for H_0.

For comparing LAVI values across frequencies (Fig. 3 A,D) we adopted a cluster-permutation approach (*56*, *57*). This non-parametric method is appropriate to control the family-wise error rate since values of neighboring frequencies are not independent from each other. We normalized the values of each subject by subtracting the median across frequencies. Then, we computed the *t* test at each frequency. After computing *t* values, we clustered neighboring points exceeding a significance level of $\alpha = .05$ and summed the *t* values of each cluster. This sum served as the value for comparison in the cluster-level statistics. We then created 1000 permutations of data with shuffled labels (i.e., eyes open or closed in Fig. 3A or medication On or Off in Fig. 3D), and took the *t* sum of the largest cluster in each permutation. We considered clusters in the original data as significant if their summed *t* values were higher than 99% or lower than 1% of the shuffled distribution (that is, $p<0.01$, two-tailed). Cluster-permutation analysis of amplitude covariation (Fig. 3B) was calculated using similar parameters, but here the *t*-test was performed between trialed data (green and blue traces) and the covariance over the whole session (grey trace). Significant clusters of WTPL in time and frequency (fig. 2E-G) were defined with *t*-sums computed relative to a baseline with no TMS pulses (-1 to -0.5 s), over 64 repetitions (2^6, maximal permutation possible with six subjects).

Supplementary Text

Parametrical effects on rhythmicity measures

As mentioned above (Lagged Angle Vector Index (LAVI) section of methods), the founding principle underlying the lagged coherence (LC) analysis is that "real" oscillations are repetitive. Therefore, their periodic waveforms should allow for the prediction of future phases based on the phase of the present one. Based on this principle, Fransen and colleagues (*20*) defined *rhythmicity* as "the consistency of the phase relations between time points that are separated by some interval (lag)". Practically, rhythmicity (computed with LC) measures the predictability of future phases based on the current one: the better future phases can be predicted, the more rhythmic the signal. Fransen et al also noted, that LC varies as a function of both frequency and lag. LC peaks at frequencies corresponding to "canonical bands" (Fig. 1), and decreases with increasing lag (fig. S5A, example from 60 sec recordings from one participant in dataset III).

Based on this dependence of LC on both frequency and lag, several studies (*20*–*22*) quantified how oscillatory an activity in a specific band is based on the "lifetime" of the LC. That is, for how long (i.e., for how many lags) does the LC exceed a threshold. However, two difficulties arise when adopting this approach: first, the threshold has to be calculated for each frequency separately, which undermines inter-frequency comparisons (*21*). Second, it requires computing the LC for numerous lags (e.g. 0 to 20 cycles in steps of 0.1, summing to 201 lags (*21*) or 2 to 7 cycles, summing to 51 lags (*22*)). This makes LC computationally very intensive.

Looking for a computationally fast way to utilize rhythmicity to define oscillatory bands, we investigated how different parameters affect LAVI. First, we noticed that the dynamic range of the rhythmicity is lower in short (<=1 cycle) and long (>=3 cycles) lags compared to lags between 1 and 2 cycles (fig. S5B). This effect is due to a ceiling effect in short lags and a floor effect in long lags. Importantly, the median (across frequencies) is lag-dependent and is highly stable across participants (fig. S5C, 60 sec EEG from N=127 participants, datasets I-IV).

Another parameter that affects the median of LAVI is the duration of the sliding window used to calculate the time-frequency transform. We used Wavelet transform, hence this parameter is reflected in the length of the Wavelet, measured in cycles per frequency. The wider the Wavelet, the higher the assessed rhythmicity (fig. S5D). Based on the finding that the LAVI median is highly stable across participants (e.g., standard deviation of 0.01, when using lag=1.5 cycles and Wavelet width =5 cycles), and depends on parameters controlled by the experimenter, we developed an approach to assess band borders based on one lag. That is, instead of measuring how rhythmicity changes over time relative to a baseline time-point, we measure how rhythmicity in each frequency changes relative to the median, in one time-point. We found that using a lag of 1.5 cycles and Wavelet of 5 cycles (arrows in fig S5C and S5D) allows estimation of rhythmicity that is computationally efficient, stable across participants, and offers good dynamic range (median of 0.4, that allows frequency to go above and below the median, without ceiling and floor effects).

Importantly, the median of LAVI depends on the lag and wavelet width, regardless of its source. This can be demonstrated with analysis of surrogate (random) data with spectral characteristics similar to the characteristic of neurophysiological data. In general, the power of the electrophysiological signal is inversely proportional to the frequency, or $P = 1/f^{\alpha}$, with P designating Power and the fractal α represent how steeply the power decreases. In brain signals, the fractal (also called the aperiodic component) is predominantly between 0.5 and 2, which is representative for signals dubbed "pink noise" (in the data analysed for this manuscript, out of 1150 recording sites, 82.4% had $0.5 <= \alpha <=2$, fig S5E). Leveraging this feature, we characterized the rhythmicity of data with similar pink-noise characteristics as our recorded data, but with shuffled (that is, random) phases, using the IAAFT algorithm (*43*–*45*). Starting with raw EEG data from participants, we calculated the aperiodic component of the signal by fitting a power function (fig. S5F). Then, we used the fit as the spectrum input to the IAAFT algorithm (fig. S5G). Finally, we computed the rhythmicity (LAVI) of both the original and surrogate data. As shown in fig. S5H, the rhythmicity curves of both "real" and surrogate data share the same median (~0.4, when using lag = 1.5 cycles and Wavelet width = 5 cycles). However, while the “real” data exhibits fluctuations with distinct peaks and troughs, the surrogate (“pink”) data fluctuates much less. We further utilized this finding to define noise levels of per-subject LAVI, treating the median as the baseline and matched pink-noise fluctuations as noise-floor. This approach allows statistical significance inference of each band (see ABBA above).

Notably, fluctuations in LAVI can be affected by how oscillatory or bursty the data is in specific frequencies, but also from other parameters. These parameters can be exploited do define the noise-floor. First, the higher the aperiodic exponent (α), the higher the noise, especially in low frequencies (fig. S5I). Second, noise level decreases (and in fact, accuracy increases) with increased sampling frequency. This effect becomes more prominent with higher frequencies, since the sampling frequency defines how many samples are there in each cycle, and hence the range of possible phases that can be measured (fig. S5J). Finally, the total duration of the recorded session affects noise levels in low frequencies (fig. S5K). Based on this parameterization, one can generate a table containing expected noise levels based on given aperiodic exponent, sampling frequency, and session duration. Generating such table requires simulating at least 20 repetitions of pink-noise for each parameter combination (to allow bootstrapping with α=0.05). This process can be time consuming, but carries the advantage of after being done once, the table can be used with all datasets with similar experimental conditions, thus speed up analysis. We make the table created for this manuscript, along with the code used to generate it, publicly available.

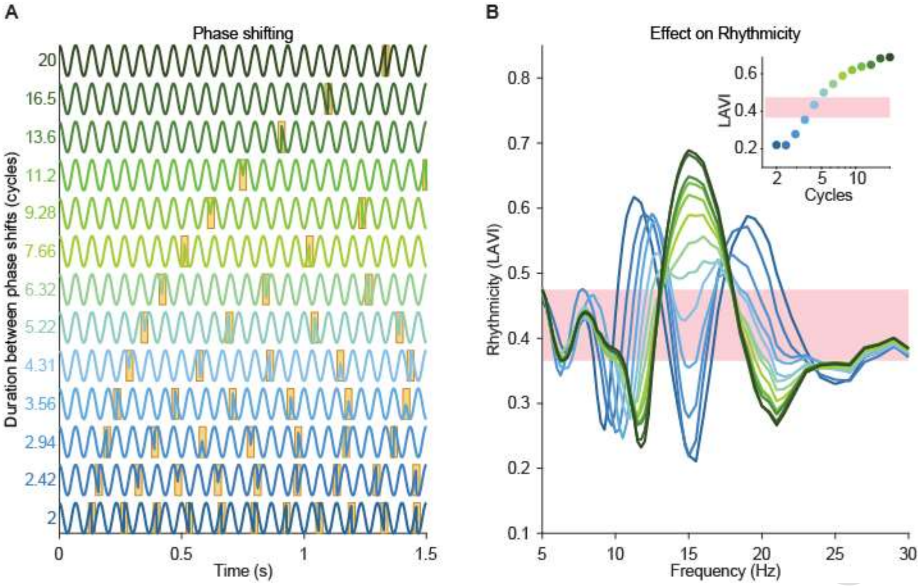

Fig. S1. The Lagged Angle Vector Index (LAVI) measures rhythmicity.
In each frequency, LAVI reflects how sustained the oscillation is over the session: sustained oscillations receive high rhythmicity values, while frequent phase shifts reduce LAVI. For direct demonstration of the effect of sustainability on LAVI, we flipped the sign of the phase of the 15 Hz component of pink-noise every set amount of cycles ranging from 2 to 20. (**A**) Simulated signal, filtered at 15 Hz, arranged from “ephemeral” (blue) to “rhythmic” (green). Phase-shifts are marked in gold. (**B**) The LAVI profile over frequencies. Colour of traces corresponds to (**A**). Pink shading corresponds to the noise, estimated as the minimal and maximal LAVI values of the pink-noise data (without filter weight adjustment at 15 Hz). Inset: LAVI values at the modulated frequency (15 Hz).The signal becomes more rhythmic than noise around four cycles. Note that increasing (decreasing) the rhythmicity in one band decreases (increases) rhythmicity in neighbouring bands. This can be caused by interference. However, peaks and troughs in physiological data are above and beyond this effect (for more details, see fig. S3).

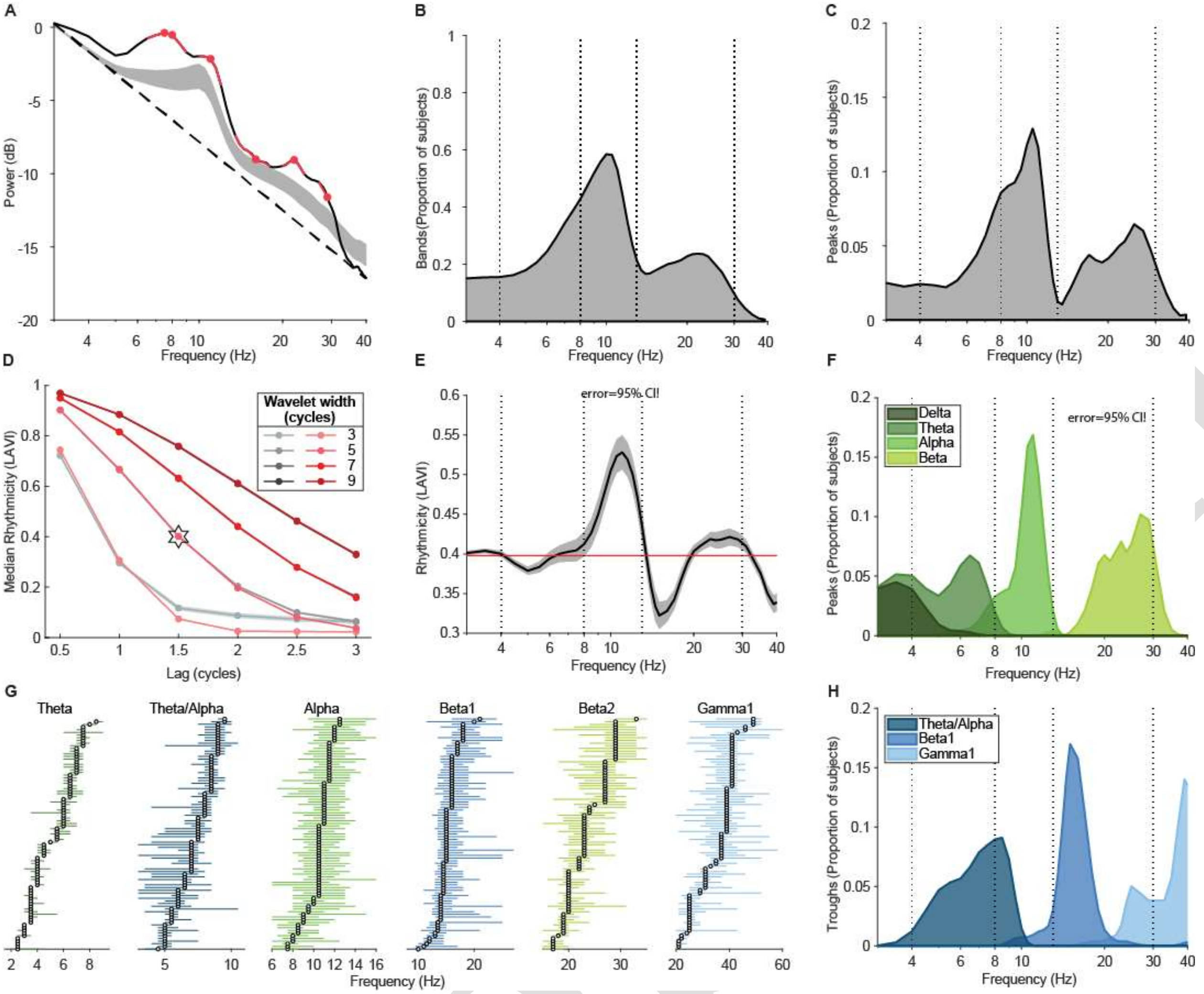

Fig. S2. Band segregation using power and rhythmicity.

(**A**) Brainwave bands are commonly defined as bumps above the 1/*f* aperiodic component. Black trace: power spectrum of one subject (same as in Fig. 1C-D). Dashed line: the 1/*f* fit. Pink: bands detected using an iterative Gaussian-fit algorithm (specparam, formerly fooof, ref. S18). Grey shading: 95% confidence-interval (CI) of population power (N = 90 participants from datasets I, II, and IV). Group averaged of bands detected by specparam are presented in (**B**), and peaks in (**C**). Dashed lines in (**B**), (**C**), (**E**), (**F**), and (**H**) at 4,8,12, and 30 Hz denote borders between canonical bands (ref. 17). (**D**) Median rhythmicity levels are stable across participants and data types. Grey (pink) traces denote the mean and shades the 95% CI of the median of 90 subjects (pink-noise) using different lags and wavelet widths. Note that with 5 or more wavelet length, and 2 or less cycle lags, noise and data are indistinguishable. This allows using surrogate data to estimate noise floor and significance levels, as further discussed in Supplementary Text, Parametrical effects on rhythmicity measures, and fig. S4. Star denotes the values used throughout the manuscript. (**E**) Black: Mean ± 95% CI of the population (N = 90) rhythmicity values. Pink: mean ± 95% CI of the medians of each subject. (**F**) Population summary of significantly (p<0.05) sustained peaks detected by ABBA. (**G**) Forest plot of significant bands. Circle: peak (or trough) of each subject. Green horizontal lines: limits of rhythmic bands. Blue horizontal lines: limits of arrhythmic bands. Note that although the ranges of bands are stable and agree with canonical bands (ref 17), there is a considerable degree of inter-subject variability, which can lead to erroneous band-definition and deems individual band definition necessary. (**H**). Population summary of significantly (p<0.05) transient peak-frequencies (i.e., troughs in LAVI) detected by ABBA.

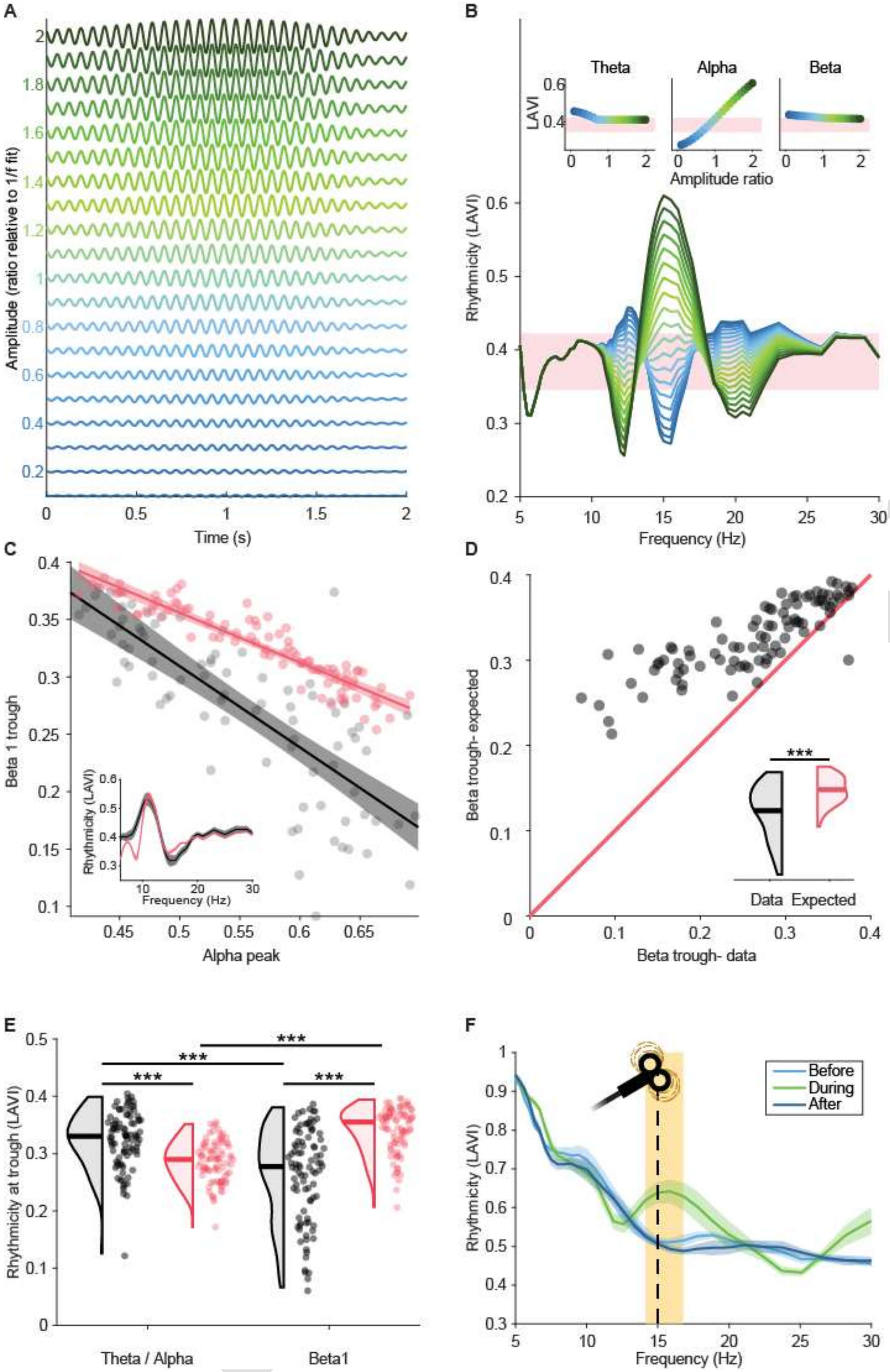

Fig. S3. Transient bands are more arrhythmic than expected by interference shadows from neighbouring rhythmic bands. (**A-B**) Potential cross-frequency effects on the rhythmicity profile. Reducing the power in one frequency, e.g. by filtering (**A**, blue traces) reduces the rhythmicity in this frequency below expected by pink-noise (**B**), but also increases rhythmicity in neighbouring frequencies. Conversely, increasing the power (green traces) increases rhythmicity in the manipulated frequency and reduces rhythmicity in the neighbouring frequencies. This interference shadow can theoretically be the (artefactual) source of troughs in the rhythmicity profile that would be erroneously defined as arrhythmic bands.

(**C**) Rhythmicity levels (LAVI) at the alpha peak vs. the beta1 trough of 90 participants (black) or pink-noise (pink). To generate the pink noise distribution, we created 90 instantiations of 120 s pink noise, each with power at 11 Hz (alpha) randomly chosen between 1.05 to 2.25 of the original (1/*f*) value. Dots: individual subjects/ noise instantiations. Lines: linear regression. Shades: 95% prediction intervals. Data: Pearson ρ=-0.832, $p<10^{-23}$. Noise: ρ=-0.927, $p<10^{-38}$. Inlet: Population mean ± 95% CI of rhythmicity values. (**D**) Based on the alpha-to-beta1 linear regression of pink-noise, we compared the beta1 rhythmicity levels measured in the data (abscissa) to the beta1 levels expected given the alpha peak levels of each participant (ordinate). Note that 89 out of 90 subjects (99%) were above the unity line, indicating that their beta1 trough is lower than expected by interference shadows from alpha ($t_{89}=11.8$, $p<10^{-19}$, inlet). (**E**) Beta1 trough is more arrhythmic than expected by alpha interference. For each subject we created a 3 min surrogate pink-noise trace, with matched aperiodic component and alpha power (10 Hz) matching the original (non-fit) value, and extracted the rhythmicity levels at the trough between theta and alpha and the beta1 trough of both data (black) and surrogate (pink). Rainclouds show the full distribution. Horizontal lines: median. Two-way ANOVA (band and data type): main effect for band: $F_{1,356}=0.94$, $p=0.33$; main effect for data type: $F_{1,356}=14.1$, $p<10^{-3}$; interaction: $F_{1,356}=95$, $p<10^{-19}$. ***- p<0.001, post-hoc t-test with Bonferroni correction. The significant interaction indicates that the artefactual interference effect of rhythmic alpha is expected to be stronger on lower frequencies, but in the data the beta1 trough is more arrhythmic than expected by noise and in comparison to the theta-alpha trough. (**F**) Repetitive TMS increases rhythmicity in the stimulated frequency, but the interference shadow does not reach significance. The rhythmicity levels before (light blue), during (green) and after (dark blue) 6 rhythmic TMS stimulations at 15 Hz (dashed line). Shaded area: rhythmicity during is different than before/ after ($p<0.05$, cluster permutation test).

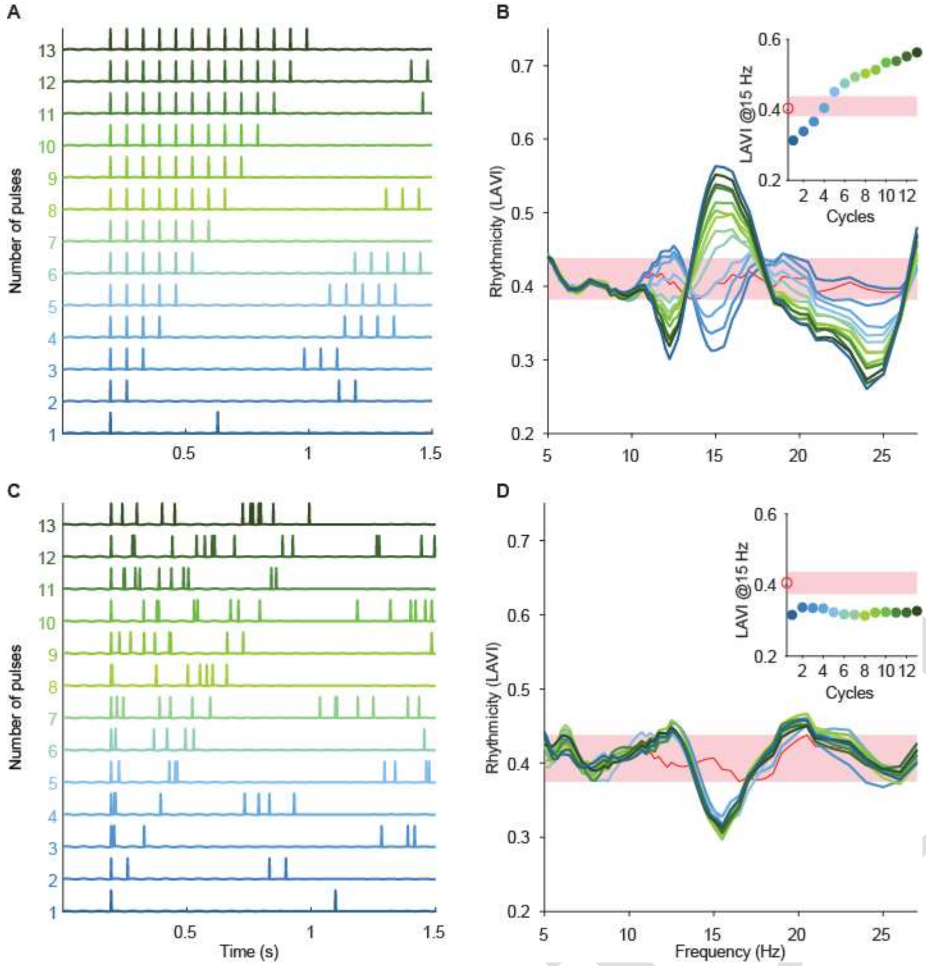

Fig. S4. The effect of repeating pulses on rhythmicity.

(**A-B**): Rhythmic pulses, (**C-D**): Arrhythmic pulses. (**A, C**): Simulations design. Synchronized (**A**) or asynchronized (**C**) transient inputs were simulated as trains of strong pulses. The first and last inputs in a train were time locked to the same duration, whereas the intervals between inputs within trains were constant in (**A**) and randomized in (**C**). (**B,D**): The response of the rhythmicity profile to rhythmic (**B**) or arrhythmic (**D**) inputs. Colour code identical to main Fig. 2C. Note rhythmicity levels higher than expected by noise with 5 or more synchronized pulses (**B**), but no effect of number of pulses on rhythmicity with asynchronized pulses (**D**).

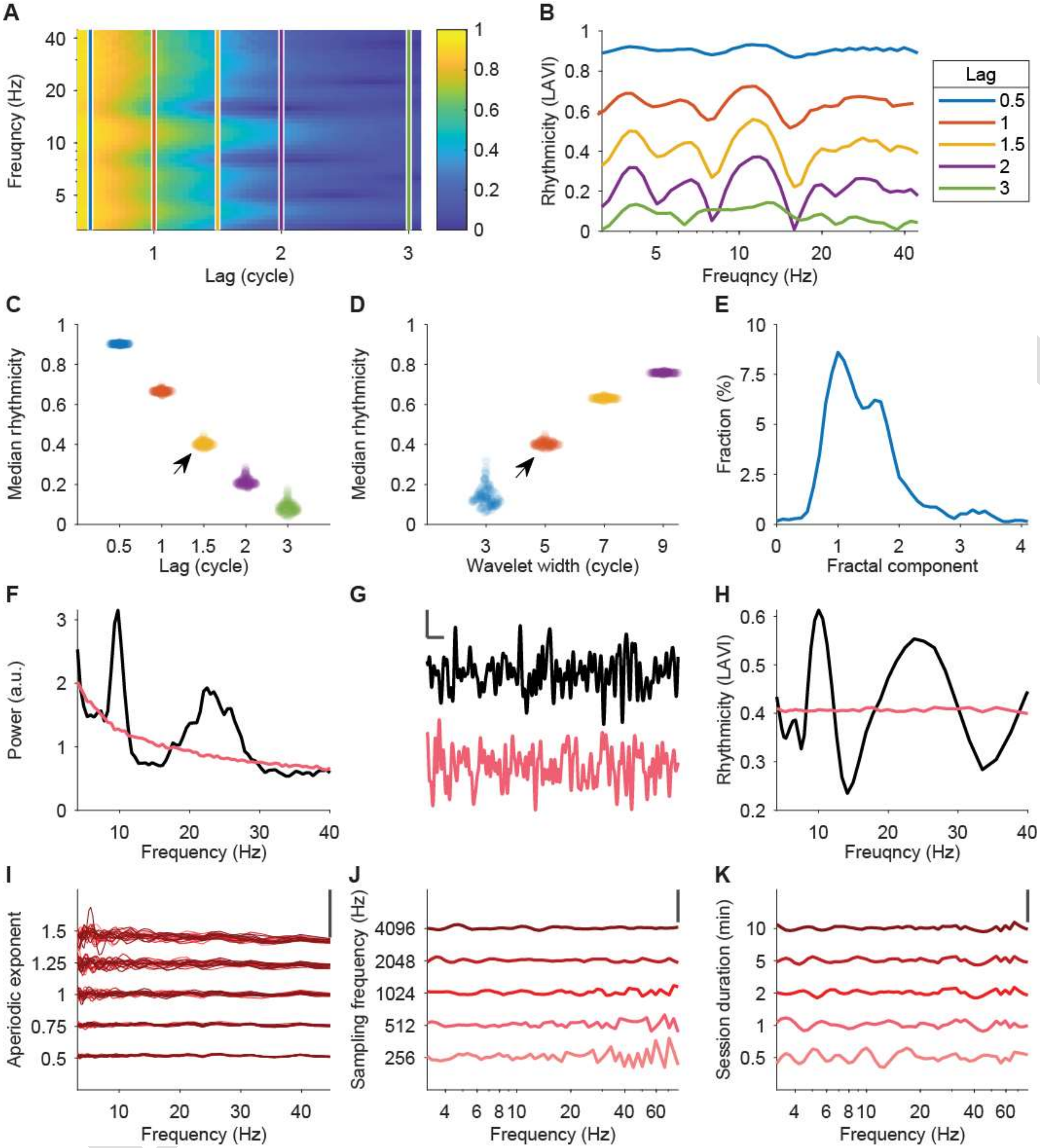

Fig. S5. Parametrical choices allowing fast frequency-dependent rhythmicity detection.
(**A**) A common practice in measuring rhythmicity is to plot the lagged-coherence as a function of both lag and frequency, and then find bands with relatively longer durations with higher values. Example from one participant from dataset III. Colour map represents rhythmicity (LAVI). Coloured lines correspond to specific lags plotted in **B**. (**B**). The dynamics of LAVI in different lags keeps pattern, with ceiling and floor effects in short and long lags, respectively. (**C**) The LAVI median is stable over participants. The median (over frequencies) of each of the N=127 participants (dots, colour code same as **B**) is plotted as a function of lag. For all lags, the wavelet width was kept at 5 cycles. Note the relatively low variation within lags. (**D**) Similar to **C**, with varying wavelet lengths. Lag = 1.5 cycles for all. Arrows in **C** and **D** represent the parameters used throughout this manuscript. (**E**) Aperiodic component distribution. Note that most values are between 0.5 and 2, corresponding to "pink" noise. (**F**) The power spectrum density of one subject, and the aperiodic component resolved with power fit. This fit was injected into the IAAFT to generate the surrogate data. (**G**) Raw traces of the original data (black) and surrogate (pink). Vertical bar: 10 µV. Horizontal: 0.1 s. (**H**) The LAVI of the real (black) and surrogate (pink) data. Note that the real data's LAVI has peaks and troughs corresponding to the rhythmicity structure, while the surrogate's LAVI is relatively flat. (**I-K**) Parametric effects on LAVI noise levels. Aperiodic exponent (**I**), Sampling frequency (**J**), and Session duration (**K**) influence noise levels on different frequencies in a predictable manner. This allows generating simulations-based significance tables. Bars: LAVI=0.1.